Mapping Evapotranspiration with High Resolution Aircraft Imagery over Vineyards Using One and Two Source Modeling Schemes

Ting Xia[1,2], William P. Kustas[2], Martha C. Anderson[2], Joseph G. Alfieri[2], Feng Gao[2], Lynn McKee[2], John H. Prueger[3], Hatim M. E. Geli[4], Christopher M.U. Neale[5], Luis Sanchez[6], Maria Mar Alsina[6], Zhongjing Wang[1,7]

[1]{Department of Hydraulic Engineering, Tsinghua University, Beijing, 100084, China}

[2]{USDA-ARS, Hydrology and Remote Sensing Laboratory, Beltsville, MD, USA}

[3]{USDA-ARS, National Laboratory for Agriculture and the Environment, Ames, IA, USA}

[4]{Department of Civil and Environmental Engineering, Utah State University, Logan, UT, USA}

[5]{Robert B. Daugherty Water for Food Institute, University of Nebraska-Lincoln, NE, USA}

[6]{E. & J. Gallo Winery, Viticulture, Chemistry and Enology, Modesto, CA 95353, USA}

[7]{State Key Laboratory of Hydro-Science and Engineering, Tsinghua University, Beijing, 100084, China}

Correspondence to: William P. Kustas (bill.kustas@ars.usda.gov)

Abstract

Thermal and multispectral remote sensing data from low-altitude aircraft can provide high spatial resolution necessary for sub-field (≤ 10 m) and plant canopy (≤ 1 m) scale evapotranspiration (ET) monitoring. In this study, high resolution (sub-meter scale) thermal infrared and multispectral shortwave data from aircraft are used to map ET over vineyards in central California with the Two Source Energy Balance (TSEB) model and with a simple model having operational immediate capabilities called DATTUTDUT (Deriving Atmosphere Turbulent Transport Useful To Dummies Using Temperature). The latter uses contextual information within the image to scale between radiometric land surface temperature (T_R) values representing hydrologic limits of potential ET and a non-evaporative surface. Imagery from five days

throughout the growing season is used for mapping ET at the sub-field scale. The performance of the two models is evaluated using tower-based measurements of sensible (H) and latent heat (LE) flux or ET. The comparison indicates that TSEB was able to derive reasonable ET estimates under varying conditions, likely due to the physically based treatment of the energy and the surface temperature partitioning between the soil/cover crop inter-row and vine canopy elements. On the other hand, DATTUTDUT performance was somewhat degraded presumably because the simple scaling scheme does not consider differences in the two sources (vine and inter-row) of heat and temperature contributions or the effect of surface roughness on the efficiency of heat exchange. Maps of the evaporative fraction (EF=LE/(H+LE)) from the two models had similar spatial patterns but different magnitudes in some areas within the fields on certain days. Large EF discrepancies between the models were found on two of the five days (DOY 162 and 219) when there were significant differences with the tower-based ET measurements, particularly using the DATTUTDUT model. These differences in EF between the models translate to significant variations in daily water use estimates for these two days for the vineyards. Model sensitivity analysis demonstrated the high degree of sensitivity of the TSEB model to the accuracy of the T_R data while the DATTUTDUT model was insensitive to systematic errors in T_R as is the case with contextual-based models. However, it is shown that the study domain and spatial resolution will significantly influence the ET estimation from the DATTUTDUT model. Future work is planned for developing a hybrid approach that leverages the strengths of both modeling schemes and is simple enough to be used operationally with high resolution imagery.

1 Introduction

As a key component of the land hydrological, energy and biogeochemical cycles, evapotranspiration (ET) provides important information about terrestrial water availability and consumption (Evett et al., 2012). Detailed knowledge of spatial ET distributions (especially in near-real time) at field or finer scale is particularly useful in precision agricultural water management (Anderson et al., 2012a; Sánchez et al., 2014). This is especially relevant as the need to increase food production for a growing human population is hindered by the reduced availability of freshwater in many water limited regions, which potentially will be exacerbated with a changing climate. Remote sensing techniques are considered to be one of the few reliable methods for mapping and monitoring ET at watershed and regional scales (Su, 2002; Kustas and

Anderson, 2009) since they provide a means for detecting changes in vegetation and soil moisture conditions at field scale affecting ET over space and time.

Over the past several decades, numerous satellite products have been used in ET estimation and monitoring. Among them, medium to moderate spatial resolution (100-1000 m) satellite data, e.g., from Landsat and the MODerate resolution Imaging Spectrometer (MODIS), have been applied with models for mapping ET at field to watershed and regional scales with some success (Anderson et al., 2012b; Cammalleri et al., 2013). [In this paper we define satellite imagery with resolution on order of ~100 m as "medium resolution" and 1000 m as "moderate resolution" to distinguish from high resolution imagery with meter-scale spatial resolution.] However, as water resources become more limited, there is a greater need for precision agricultural management at the field/subfield-scale, particularly for high-valued or specialty crops (Zipper and Loheide II, 2014), and moderate resolution data are too coarse to inform variable rate application of water or nutrients within a field. In addition, obtaining both high spatial and temporal resolution data is not feasible with the current satellite constellation since medium resolution earth observations have a long (two or more weeks) revisit cycle, particularly when considering cloud cover (Cammalleri et al., 2013).

Remote sensing data from low altitude aircraft, especially from unmanned aerial vehicles (UAVs), can potentially provide the needed spatial and temporal frequency for precision agriculture applications. Despite the fact that development of airborne scanner-derived thermal imagery for irrigation applications had begun back in the 1970s (Jackson et al., 1977), it is not until the last few years that very high resolution data are being considered for precision agricultural applications. This is due to the technological advances that have allowed rapid integration and processing of high-resolution data from cameras mounted on aircraft and more recently on-board UAVs (Zarco-Tejada et al., 2013). Current applications of high resolution thermal remote sensing data are mainly focused on detecting and mapping crop water status (Berni et al., 2009a; Gonzalez-Dugo et al., 2012; Zarco-Tejada et al., 2012) since canopy temperature has historically been used as an indicator of water stress (Jackson et al., 1981; Gardner et al., 1981; Fuentes et al., 2012). Sub-meter resolution thermal imagery is able to retrieve pure canopy temperature, minimizing soil or other background thermal effects (Leinonen and Jones, 2004; Zarco-Tejada et al., 2013).

Spatially distributed ET can be obtained using remote sensing-based models with varying degrees of complexity and utility (Kalma et al., 2008). In terms of treatment of the energy exchange with the surface, the thermal remote sensing-based ET models can be generally classified as one source (Bastiaanssen et al., 1998; Su, 2002; Feng and Wang, 2013) and two source (Norman et al., 1995; Kustas and Norman, 1999; Long and Singh, 2012; Yang and Shang, 2013) parameterizations depending on whether they treat a landscape pixel as a composite/lumped surface or explicitly partition energy fluxes and temperatures between soil and vegetation. These models are based on solving the surface energy balance and adopt radiometric surface temperature (T_R) as a key boundary condition (Kustas and Norman, 1996).

A commonly used method in one source models is the contextual scaling approach, which uses T_R and vegetation amount (the normalized difference vegetation index, NDVI, or fractional vegetation cover, f_c) as proxy indicators of ET (Bastiaanssen et al., 1998; Su, 2002; Allen et al., 2007; Carlson et al., 1994; Jiang and Islam, 1999). Accurate identification of extreme hydrologic limits, i.e., potential ET (cold/wet limit) and the largest water stress condition (hot/dry limit), is essential for proper scaling of the surface condition (e.g., the aerodynamic and air temperature difference, dT, and evaporative fraction, EF) of the other pixels between these extremes. Examples include the Surface Energy Balance Algorithm for Land (SEBAL) (Bastiaanssen et al., 1998), the Mapping Evapotranspiration with Internalized Calibration (METRIC) model (Allen et. al., 2007), the triangle model (Carlson et al., 1994), and the satellite-based energy balance algorithm with Reference Dry and Wet limits (REDRAW) (Feng and Wang, 2013).

With UAV imagery, the pixel resolution can be very fine (i.e., 10^0 cm – 10^0 m) in order to map the variability in crop condition within a field. This typically restricts the size of the area or field being monitored and hence reduces the likelihood of sampling the extremes in ET rates (i.e., ET ~0 and ET at potential). This issue was raised by Zipper and Loheide II (2014) who indicated that thermal-based ET models relying on extreme limits are not applicable at field scales since in agricultural landscapes vegetation cover within a field is fairly homogeneous and ideal extreme limits may be difficult to identify, especially during mature crop periods when the canopy is nearly closed. They developed a mixed-input approach combining high resolution airborne and Landsat imagery with local meteorological forcing in a surface energy balance model they called High Resolution Mapping of EvapoTranspiration (HRMET). HRMET combines a two-source

modeling approach for estimating available energy between the soil and vegetation elements but uses a single-source scheme for estimating the soil+canopy system *H*, with LE solved by residual.

On the other hand, the contextual scaling approach can greatly simplify model computations and input data requirements (Carlson, 2007), and can reduce ET retrieval errors due to bias errors in T_R and meteorological inputs such as air temperature and wind speed (Allen et al., 2007). This facilitates near real-time operational applications for ET monitoring. In the DATTUTDUT (Deriving Atmosphere Turbulent Transport Useful To Dummies Using Temperature) modeling scheme introduced by Timmermans et al. (2015), land surface temperature is the only input needed for ET estimation. DATTUTDUT solves for ET by scaling the evaporative fraction, EF, between the extreme values associated with potential (cool/wet pixel) and zero (hot/dry pixel) ET. The main concept of DATTUTDUT is similar to the S-SEBI (the Simplified Surface Energy Balance Index) proposed by Roerink et al. (2000); however, DATTUDDUT has a more simplified scheme to obtain radiometric temperature end-members and radiation-related factors. Although these types of contextual scaling methods have been tested over a variety of landscapes using mainly moderate resolution remote sensing data, their applicability and performance in retrieving surface fluxes and ET at the high resolution/sub-field scale, and potential problems or behavior at the sub-field scale have not been adequately tested.

The Two Source Energy Balance (TSEB) scheme originally proposed by Norman et al. (1995) and modified by Kustas and Norman (1996, 1999, 2000), has proven to be fairly robust for a wide range of landscape and weather conditions (Li et al., 2005; Kustas and Anderson, 2009; Colaizzi et al., 2012a). Unlike single-source models based on contextual scaling approaches, the TSEB model contains a more detailed treatment of the radiative and flux exchange between soil and vegetation elements without the requirement of extreme hydrological limits existing within the scene. Consequently, TSEB is still effective when applied over homogeneous landscapes and environmental conditions.

The performance of TSEB and single-source models using T_R/ET extremes (e.g., SEBAL, METRIC, Trapezoid Interpolation Model (TIM)) has been compared over a corn and soybean region in Iowa during SMACEX (French et al., 2005; Choi et al., 2009), sub-humid grassland and semi-arid rangeland during SGP '97 and Monsoon '90 (Timmermans et al., 2007), as well as a cotton field in Maricopa, Arizona (French et al., 2015). These studies demonstrated that both

TSEB and the single-source models can reproduce fluxes with similar agreement to tower-based observations, yet they did reveal significant discrepancies in the ET patterns or spatial distributions especially in areas with bare soil or sparse vegetation. In general, these model inter-comparisons have mainly used medium resolution satellite imagery such as Landsat and Advanced Spaceborne Thermal Emission and Reflection radiometer (ASTER). French et al. (2015) conducted model comparison using both Landsat and aircraft data, and concluded that daily ET estimations were similar at high and medium spatial resolutions.

However, more detailed comparisons between simple one-source contextual-based schemes versus more complex two-source models using high resolution imagery over different surfaces are still needed to fully understand the strengths and weaknesses of both modeling schemes. Such intercomparisons can facilitate development of hybrid schemes that leverage the strengths of different methodologies (e.g., Cammalleri et al., 2012), while incorporating simplications for routine application with airborne imagery. The purpose of this paper is to conduct an inter-comparison of TSEB with the very simple contextual-based DATTUTDUT model that can be easily applied operationally using high resolution thermal and multispectral shortwave imagery for sub-field scale ET estimation. The inter-comparison is conducted over two vineyard fields having significantly different biomass in central California. ET estimates from the TSEB and DATTUTDUT models are compared in detail within the contributing source-area of the flux tower in each field, and the spatial patterns of modeled ET are compared throughout the whole vineyard field. Additionally, a sensitivity analysis of key inputs to the two models is conducted, providing insight into the potential for precision agricultural water resource management applications using such high resolution earth observations.

2 Model overview

2.1 TSEB model

The TSEB model, developed by Norman et al. (1995), partitions surface temperature and fluxes into soil and vegetation components. Detailed formulations used in TSEB can be found in Kustas and Norman (1999) and Li et al. (2005, 2008). In the TSEB model, the surface energy budgets are balanced for both the soil and canopy components of the scene:

$$R_{\mathrm{n}} = R_{ns} + R_{nc} = H + \mathrm{LE} + G \qquad (1)$$

$$R_{ns} = H_s + LE_s + G \quad (2)$$

$$R_{nc} = H_c + LE_c \quad (3)$$

where R_n is net radiation (W m^{-2}), H is sensible heat flux (W m^{-2}), LE is latent heat flux (W m^{-2}), and G is soil heat flux (W m^{-2}). Subscripts s and c represent the soil and canopy flux components, respectively. Component R_n is combined with the component temperature (Colaizzi et al., 2012b; Song et al., 2016):

$$R_{ns} = \tau_l L_d + (1-\tau_l)\varepsilon_c \sigma T_c^4 - \varepsilon_s \sigma T_s^4 + \tau_s (1-\alpha_s) S_d \quad (4)$$

$$R_{nc} = (1-\tau_l)\left(L_d + \varepsilon_s \sigma T_s^4 - 2\varepsilon_c \sigma T_c^4\right) + (1-\tau_s)(1-\alpha_c) S_d \quad (5)$$

where L_d and S_d are incoming longwave and shortwave radiation (W m^{-2}), τ_l and τ_s are the longwave and shortwave radiation transmittances through the canopy (-). ε, α and T are surface emissivity (-), surface albedo (-) and surface temperature (K) with subscripts s and c represent the soil and canopy. σ is the Stefan-Boltzmann constant (~5.67×10^{-8} W m^{-2} K^{-4}). S_d is either computed using sun-earth astronomical relationships under clear-sky conditions as done by DATTUTDUT (see below) or measured from a nearby weather station, and L_d is either measured or often computed using formulas based on weather station observations of air temperature and vapor pressure (i.e., Brutsaert, 1975).

T_R is partitioned into component soil, T_s, and canopy, T_c, temperatures based on the fractional vegetation cover (f_c):

$$T_R \approx \left[f_c(\theta) T_c^4 + (1 - f_c(\theta)) T_s^4\right]^{1/4} \quad (6)$$

where $f_c(\theta)$ is the vegetation cover fraction at the thermal sensor view angle θ. A clumping factor, Ω, is adopted in the $f_c(\theta)$ calculation to account for the row structure of vineyards (i.e., vine biomass concentrated along trellises) using a formulation from Campbell and Norman (1998):

$$f_c(\theta) = 1 - \exp\left[\frac{-0.5\Omega(\theta) LAI}{\cos(\theta)}\right] \quad (7)$$

where LAI is leaf area index, which is often estimated from NDVI using an empirical LAI~NDVI relation (Anderson et al., 2004). When calculating the flux component H, "series"

and "parallel" schemes are adopted for the resistance network separately for unstable and stable conditions. Detailed formulations for the two schemes can be found in Norman et al. (1995) and Kustas and Norman (1999). LE_c is initially estimated using a Priestley-Taylor formulation:

$$LE_c = \alpha_{PT} f_G \frac{\Delta}{\Delta + \gamma} R_{nc} \quad (8)$$

where α_{PT} is Priestley-Taylor parameter, which may vary within different vegetation and climate conditions (Norman et al., 1995; Kustas and Norman, 1999; Kustas and Anderson, 2009). In this paper, the initial value of α_{PT} is 1.26. f_G is the LAI fraction that is green with active transpiration. Δ is the slope of the saturation vapor pressure-temperature curve (Pa K^{-1}) and γ is the psychrometric constant (Pa K^{-1}). G is parameterized as a fraction of R_{ns} by:

$$G = cR_{ns} \quad (9)$$

where c is the empirical coefficient which tends to be constant during midmorning to midday period.

With the above model formulations, energy fluxes for both soil and canopy can be solved. Important model inputs for TSEB include T_R, fractional canopy cover condition (often related to NDVI), and a land use map providing canopy characteristics (mainly vegetation height and leaf width) obtained using remote sensing imagery. Ancillary meteorological data required in TSEB include air temperature, vapor pressure, atmospheric pressure, and wind speed.

2.2 DATTUTDUT model

The DATTUTDUT model is an energy balance model that estimates surface energy fluxes solely from radiometric surface temperature observations acquired over the area of interest. This model assumes that T_R is an important indicator for the surface status, and scales key parameters for flux estimation by T_R between the extremes of a cool/wet pixel with ET at the potential rate and hot/dry pixel where there is essentially no ET. Detailed model formulations are described in Timmermans et al. (2015). Similar to other energy balance models, R_n is estimated by computing the net shortwave radiation and the net longwave radiation:

$$R_n = (1-\alpha)S_d + \varepsilon\varepsilon_a\sigma T_a^4 - \varepsilon\sigma T_R^4 \quad (10)$$

where ε_a is the atmosphere emissivity (-) and ε is the effective (integrated soil + canopy emissivity) emissivity. The value of S_d is obtained from the sun-earth astronomical relationships under clear-sky conditions (Allen et al., 2007; Timmermans et al., 2015). In the DATTUTDUT model, nominal values are taken for ε and ε_a for simplicity: ε_a is set to be 0.7 and ε is taken as 0.96. Air temperature, T_a (K), is assumed to be equal to the minimum T_R identified within the scene of interest. α is scaled with T_R between extreme values of 0.05 and 0.25 based on the assumption that densely vegetated objects are likely to be darker and cooler while bare objects tend to appear brighter and hotter:

$$\alpha = 0.05 + \left(\frac{T_R - T_{\min}}{T_{\max} - T_{\min}} \right) 0.2 \tag{11}$$

where T_{max} is the maximum T_R within the image, and T_{min} is the 0.5% lowest temperature in the scene. Soil heat flux is calculated from R_n with the coefficient c_G scaled between a minimum value of 0.05 for fully covered condition and maximum value of 0.45 for bare soil (Roerink et al., 2000; Santanello and Friedl, 2003):

$$c_G = \frac{G}{R_n} = 0.05 + \left(\frac{T_R - T_{\min}}{T_{\max} - T_{\min}} \right) 0.4 \tag{12}$$

Similar to α and c_G, evaporative fraction, EF, is assumed to be linearly related to T_R:

$$\mathrm{EF} = \frac{\mathrm{LE}}{\mathrm{LE} + H} = \frac{\mathrm{LE}}{R_n - G} = \frac{\mathrm{LE}}{A} = \frac{T_{\max} - T_R}{T_{\max} - T_{\min}} \tag{13}$$

where A is available energy (W m^{-2}), i.e., the difference between R_n and G. With the above formulations, LE can be calculated from A and EF, and H can be estimated as the residual to the energy balance equation.

2.3 Daily flux calculation

A common approach used to extrapolate ET from instantaneous (time of satellite overpass) to daily time scale is to assume the ratio of instantaneous LE to some reference variable remains constant during the day, which is described as "self-preservation" by Brutsaert and Sugita (1992). The reference variables typically used include A (Anderson et al., 2012b), standardized reference ET (Allen et al., 2007), solar radiation (Zhang and Lemeur, 1995), top-of-atmosphere irradiance

(Ryu et al., 2012). Cammalleri et al. (2014) compared the performances of the scale factors derived by these four reference valuables in ET upscaling at 12 AmeriFlux towers, drawing a conclusion that solar radiation was the most robust reference variable for operational applications, particularly in areas where the modeled G component of A may have high uncertainties. However, the applicability of the various reference variables may differ within areas, since the energy budget is significantly influenced by surface characteristics such as soil moisture, vegetation condition (Crago, 1996). In this study, EF (defined as the ratio of LE to A or H+LE) is assumed constant during the daytime period when solar radiation is larger than 0. The extrapolation to daytime ET using a constant EF is reasonable to apply during the main growing season period (Cammalleri et al., 2014).

The ratio of instantaneous to daytime A at the flux tower site is used to obtain daytime A for each pixel within the study area by assuming that the A ratio between pixel and flux tower is constant during the daytime. Therefore, daytime A for the pixel ($A_{p,d}$) can be derived from the pixel-based instantaneous A ($A_{p,i}$), and flux tower site values of instantaneous and daytime A ($A_{s,i}$ and $A_{s,d}$) using the following expression:

$$A_{p,d} = \frac{A_{p,i}}{A_{s,i}} A_{s,d} \tag{14}$$

Then daytime ET for each pixel ($ET_{p,d}$) can be calculated by tower observed daytime A and the EF retrieved by either TSEB or DATTUTDUT:

$$ET_{p,d} = A_{p,d} EF \tag{15}$$

and daytime H is computed as the residual in the energy balance equation.

In this study, the observed available energy from the two flux towers during the daytime period for all five days was used to extrapolate instantaneous model estimates to daytime ET totals. However, in practice tower measurements of A would not be available, so results using solar radiation to extrapolate to daytime ET will also be evaluated.

3 Data and site description

3.1 Study site

The model comparison was conducted over two vineyard sites located near Lodi in central California, using data collected as part of the Grape Remote sensing Atmospheric Profiling and Evapotranspiration eXperiment (GRAPEX) (Kustas et al., 2014). With a Mediterranean climate, this area has abundant sunshine and large day-and-night temperature differences, making it a primary wine grape producing area in California. This study focuses on two drip irrigated Pinot Noir vineyards trained on quadrilateral cordons with a 1.5m space between vines and 3.3m distance between rows. Although the drip-irrigation system was designed to apply water along the vine row uniformly across the field, it was evident that variations in soil texture and rates/amounts of water applied was not uniform in either field causing a fairly wide range in vine biomass. The north field (Site 1) has an area of about 35 ha with the flux tower located approximately half-way north-south along the eastern border of the field (38°17.3'N, 121°7.1'W), while the south vineyard (Site 2) is smaller in size, at about 21 ha with the flux tower also approximately half-way north-south along the eastern border of the field (38°16.8'N, 121°7.1'W) (see Fig. 1). The towers were deployed at these locations to maximize fetch for the predominant wind direction during the growing season, which is from the west. The vines in north field (7-8 years old) are more mature than those in south field (4-5 years old), resulting in a greater biomass/leaf area in the north field (see the LAI map for IOP2 in Fig. 4). Vine height is similar in both fields and reaches ~2.5 m in height. The vines typically leaf out in late March and grow through late August before the grapes are harvested in early September. When winter rains and soil moisture are adequate, a grass cover crop flourishes early in the growing season in the inter-row until becoming senescent starting in late May, which is typically the beginning of the dry season. During the growing season in 2013, the average air temperature was nearly 20 ℃ and the total precipitation was only about 15 mm.

3.2 Micrometeorological data

Micrometeorological instruments for measuring the meteorological and flux data were installed at both the north and south field flux tower sites in late March, 2013. The meteorological data needed for running the TSEB model include air temperature, vapor pressure, atmospheric

pressure, wind speed, and incoming solar radiation. These were all measured at approximately 5 m above local ground level (AGL) and recorded as 15 minute averages. The eddy covariance (EC) system comprised of a Campbell Scientific, Inc.[1] EC150 water vapor/carbon dioxide sensor and a CSAT3 three-dimensional sonic anemometer, both collecting data at 20 Hz producing 15-minute averages. A Kipp and Zonen CNR1 four-component radiometer measured net radiation at 6 m AGL. Five soil heat flux plates (HFT-3, Radiation Energy Balance Systems, Bellevue, Washington) buried cross-row at a depth of 8 cm recorded soil heat flux. Each heat flux plate had two thermocouples buried at 2 and 6 cm depths and a Stevens Water Monitoring Systems HydraProbe soil moisture sensor buried at a depth of 5 cm used to estimate heat storage above each plate. Both meteorological and fluxes data were measured through the whole vine growing season (April to October) in 2013. During this period (including both daytime and nighttime observations), the slope between A and H+LE is 0.83 for both two sites with coefficient of determination (R^2) on order of 0.97. This suggests an average energy balance closure of nearly 85%. In this study, the EC fluxes were closed using both the Residual (RE) and Bowen Ratio (BR) methods described in Twine et al. (2000) to ensure energy conservation.

3.3 Airborne campaigns

Three Intensive Observation Periods (IOPs) were conducted through the 2013 growing season as part of GRAPEX to capture different vine and inter-row cover crop phenological stages that may affect ET rates. During IOP1 (April 9-11, 2013; Day of Year (DOY) 99-101) the vines were just starting to leaf out and the cover crop in the inter-row was green and flourishing. By the time of IOP2 (June 11-13, DOY 162-164), the vines were fully developed with immature green grapes, while the cover crop was senescent. Grapes were beginning to ripen and reach maturity while the vines were still green and growing during IOP3 (August 6-8, DOY 218-220).

Airborne campaigns were conducted on five days (DOY 100, 162, 163, 218 and 219) over the three IOPs. Multispectral and thermal imagery were acquired over the two vineyards with the Utah State University airborne digital system installed in a single engine Cessna TU206 aircraft dedicated for research. The system consists of four ImperX Bobcat B8430 digital cameras with

[1] The use of trade, firm, or corporation names in this article is for the information and convenience of the reader. Such use does not constitute an official endorsement or approval by the United States Department of Agriculture or the Agricultural Research Service of any product or service to the exclusion of others that may be suitable.

interference filters forming spectral bands in the Blue (0.465-0.475 μm), Green (0.545-0.555 μm), Red (0.645-0.655 μm) and Near Infrared (NIR) (0.780-0.820 μm) wavelengths. The thermal infrared (TIR) images were acquired with a ThermaCAM SC640 by FLIR Systems Inc. in the 7.5-13 μm range. The aircraft-based TIR images were provided in degrees Celsius and used in this analysis without performing atmospheric correction. Details of image acquisition and processing can be found in Neale et al. (2012). In Table 1, overpass time (UTC), multispectral and thermal pixel resolution, information and aircraft altitude are listed for the overpass dates. The high spatial resolution of the visible bands (0.05 or 0.1 m, see Table 1) made it possible to distinguish vegetation pixels from non-vegetated pixels to some extent. However, with the coarser thermal pixel resolutions it was difficult to reliably distinguish pure vine canopy temperatures from background soil and/or inter-row cover crop temperatures (Fig. 1). Since the imagery for the different overpass dates have different spatial resolutions and the TSEB model resistance and radiation formulations for the turbulent and radiative exchange for the soil/cover-crop-vine system are appropriate at the plot/micrometeorological scale, both multispectral and thermal bands were aggregated to 5 m resolution for creating TSEB input fields to compute ET. This spatial resolution ensured both an inter-row and vine row would be sampled within the pixel.

The original or native pixel resolution of the thermal imagery was also used as input to DATTUTDUT.

3.4 Model input from aircraft data

The key TSEB model input data from the aircraft observations include maps of NDVI, LAI, f_c, and T_R. Auxiliary remote sensing data were required to produce multispectral reflectance and LAI maps. The original multispectral imagery from aircraft was in digital numbers (DN) and needed to be converted into reflectance. Smith and Milton (1999) introduced an empirical line method to calibrate remote sensing-derived DN to reflectance with errors of only a few percent in their case study. Berni et al. (2009b) applied the empirical line method on high resolution date obtained by UAV yielding calculated reflectances that agreed well with measurements (RMSD = 1.17 %). Since ground-based reflectance measurements were not collected for some of the airborne acquisition dates, Landsat multispectral band reflectance in the corresponding spectral bands were used to derive the empirical DN-reflectance relationships for this analysis.

Three Landsat images were used to match the three IOP dates: Landsat 7 on DOY 98 from path44-row33, Landsat 8 on DOY 163 from path43-row33, and Landsat 8 on DOY 218 from path44-row33. Reflectances for Band 5, Band 4, Band 3 from the Landsat 8 images, and Band 4, Band 3, Band 2 from the Landsat 7 image were used to derive the DN-reflectance relationship for NIR, red, and green bands, separately. All shortwave bands were calibrated and atmospherically corrected by the Landsat ecosystem disturbance adaptive processing system (LEDAPS) proposed by Masek et al. (2006).

The DN values with the original aircraft pixel resolution (Table 1) were aggregated up to 30 m resolution to match the Landsat multispectral bands resolution and the DN~reflectance relationship was derived. Visible band reflectance measurements were taken during the IOPs on DOY 162, 218 and 219 both above the vine row and over cover crop inter-row for both north and south fields. Estimated NIR, red and green band reflectance at aircraft pixel resolution are compared with reflectance measurements in Fig. 2. Using 54 data points, including the three bands for three days at both sites, estimated reflectance from aircraft data agreed well with observations having a bias (observed-model) of -1.1 % and root mean square difference (RMSD) of 4.5 %. This accuracy is comparable with that (a few percent) found by Smith and Milton (1999) and Berni et al. (2009b).

NDVI was assumed to be correlated with fractional vegetation cover and related to LAI (Carlson and Ripley, 1997). The MODIS Terra four-day composite LAI product (MCD15A3) was used to derive LAI maps at 30 m resolution using the regression tree approach introduced by Gao et al. (2012). NDVI maps were generated from NIR (Band 5) and red (Band 4) band of Landsat 8 data. This permitted the derivation of a LAI~NDVI relation at 30 m resolution which was used to create a LAI map at aircraft pixel resolution. An exponential equation was used to fit the LAI~NDVI relationship, which was able to accommodate the effect of NDVI saturation at high LAI values (Carlson and Ripley, 1997; Anderson et al., 2004). In Fig. 3, the LAI~NDVI equation is compared with ground-based LAI measurements using LiCor LAI-2000 on DOY 163 and DOY 218. The ground-based LAI measurements were derived from 5 transects running due west of the tower at 10-15 m intervals and across 4 rows from south to north. The average LAI from 5 transects represented a sampling area that was within 75 m due west of the flux tower sites. Four below vine canopy measurements were made and consisted of a LAI observation directly underneath vine plants along a row, and ¼, ½ and ¾ distance from the vine row. A LAI

image from IOP2 is displayed in Fig. 4 illustrating the significant spatial variation in LAI particularly for the north field.

Values of f_c were derived by the aircraft-based visible bands taking advantage of the high spatial resolution (0.05 to 0.1 m, see Table 1 and Fig. 1) which allowed separation of the vine canopy from the inter-row area. Pixels were classified into vegetation and non-vegetation categories by ENVI image processing software (Exelis, Boulder, CO), and then the percentage of vegetation pixels was quantified within each 5 m resolution pixel.

4 Results and discussion

4.1 Comparison of model estimates and tower data

Fluxes were modeled by both TSEB and DATTUTDUT at 5-m resolution using the spatially aggregated aircraft-based remotely-sensed observations. In addition, DATTUTDUT used the native pixel resolution of the thermal imagery since there is no specific spatial scale required by the model parameterizations. TSEB additionally estimates soil and canopy temperatures. A two-dimensional flux footprint model described by Li et al. (2008) based on Hsieh et al. (2000) was used to compute footprint-weighted aggregated model outputs for comparison with the tower-based measurements. This footprint model contains a lateral dispersion formulation to obtain a two-dimensional weighted source-area of flux from the upwind direction.

Average soil and canopy component temperatures from TSEB were compared to the aircraft-based observations for the pixels within the flux contributing source area of the towers (Fig. 5). The aircraft-based temperature observations were extracted using a classification of vegetation and non-vegetated areas generated with the high resolution visible bands to identify appropriate pixels in the thermal imagery. The aircraft thermal band had a pixel resolution on the order of 0.5 m (see Table 1), which was often slightly coarser scale than the width of the vine canopy and hence frequently resulted in a mixed pixel, combining both soil and canopy temperatures. Since obtaining purely vegetated surface temperature observations uncontaminated by background soil or cover crop temperature was difficult given the resolution of the thermal imagery, the minimum of the vegetated temperatures detected within the 5 m pixel was assumed to be a pure vegetated pixel temperature. Then within the footprint source area, the average of the non-vegetated temperatures (assumed to primarily consist of shaded and sunlit areas in the inter-row)

was taken as the observed T_s and average of the minimum vegetated temperatures from all 5 m pixels within the source area was estimated to represent the observed T_c. TSEB estimates of T_s and T_c agreed well with the aircraft thermal observations yielding a bias of 0.5 ℃ and RMSD on the order of 2.5 ℃. This accuracy was comparable with similar types of comparisons reported by Li et al. (2005), Kustas and Norman (1999, 2000), and Colaizzi et al. (2012a) which had RMSD values ranging from 2.4-5.0 ℃ for T_s and 0.83-6.4 ℃ for T_c when comparing observed to TSEB-derived component temperatures.

To assess the utility of the TSEB and DATTUTDUT models in reproducing the observed fluxes from the tower observations in the north (site 1) and south (site 2) vineyards, instantaneous modeled fluxes are compared with measurements (adjusted for closure using the RE method) in Fig. 6. Table 2 lists the statistics of model performance compared with both original and closure-adjusted measurements. Since the vines were at the very early growth stage during IOP1, and the inter-row cover crop was the main source of vegetation cover, the observed G on DOY 100 was significantly larger than other IOPs (Fig. 6).

Table 2 clearly shows that the RE closure adjustment method yields better overall agreement between measured and modeled fluxes with the average error computed as the ratio of RMSD and avereage observed flux value of ~27% for H and LE for the two sites, while the BR method has an error of ~37%; Instantaneous fluxes from TSEB (H and LE adjusted by RE method) agreed well with observations with RMSD ranging between 20-60 W m^{-2}, which is considered acceptable and similar to prior studies (e.g., Neale et al., 2012). DATTUTDUT gave estimated fluxes with relatively large errors particularly for R_n (RMSD = ~65 W m^{-2}) and LE (RMSD = ~105 W m^{-2}) for Site 1. The larger discrepancies in R_n from DATTUTDUT might be attributed to the simplifications in the net radiation computation (see Section 2.2). For DATTUTDUT, the results using 5 m pixel data indicate the significant error in LE predominantly resulst from poor performance on DOY 162 and 219 (Fig. 6b and 6e), likely because the extreme pixels automatically selected on these two days failed to represent the dryest/wettest conditions within the image (see discussion below).

Daytime integrated fluxes are compared with the tower measurements in Fig. 7 and Table 3. Available energy was slightly overestimated by the models for all the cases, with biases between -0.5 and -1.7 MJ m^{-2} d^{-1}. Again, the RE method yielded better agreement with the model

estimates of *H* and LE on a daytime scale. The LE values from TSEB at Site 1 agreed well with the observations with a bias of 0.5 MJ m^{-2} d^{-1} and RMSD of 1.1 MJ m^{-2} d^{-1} (Fig. 7a and Table 3). However LE from DATTUTDUT had larger differences with the measurements at Site 1 (bias = -1.1--1.0 MJ m^{-2} d^{-1} and RMSD = 1.9-2.0 MJ m^{-2} d^{-1}) mainly due to the poor agreement in the instantaneous LE. For 5 m resolution results, the two models were comparable in their agreement with LE measurements at Site 2, yielding a small bias of -0.5 to ~0 MJ m^{-2} d^{-1} and for both a RMSD on order of 1.7 MJ m^{-2} d^{-1}.

At both instantaneous and daytime time scales, application of DATTUTDUT with the native (finer) pixel resolution thermal imagery yielded comparable (at Site 1) or significantly greater (at Site 2) discrepancies with the tower measurements than using the 5 m pixel resolution data (see Tables 2 and 3). Changes in the agreement with the tower measurements are mainly attributable to the new hot and cold temperature pixels selected by the DATTUTDUT procedure with the finer resolution T_R data.

In practice, we will not have observations of available energy, *A*, from a flux tower for extrapolating the instantaneous ET from a single airborne observation to daytime ET, but instead are more likely to have weather station observations of incoming solar radiation, S_d. Results using S_d for extrapolating model estimates instead of flux tower measurements of *A* are listed in Table 4. In general, the differences between modeled and measured daytime ET (using RE method) increase, although not significantly for TSEB. On the other hand, discrepancies with the ET measurements for DATTUTDUT at the north vineyard (site 1) increase dramatically due to the large overestimation of instantaneous LE on DOY 162 and 219 (see Fig. 6b).

In general, the TSEB reproduced the measured fluxes with higher accuracy than did DATTUTDUT, both at the instantaneous and daytime temporal scales. It is hypothesized that this likely results from a better physical representation of the energy and radiative exchange within TSEB, since it explicitly considers differences in soil and vegetation radiation and turbulent energy exchange and affects on the radiative temperature source (French et al., 2005; Timmermans et al., 2007). Flux estimation from single-source models based on the use of ET extremes will be sensitive to the selection of extreme end-member T_R pixels (Feng and Wang, 2013; Long and Singh, 2013), and actual extremes might not exist when applying such models to to small vineyards that are uniformly irrigated and managed as in this study. This may be a key

factor that caused the fluxes from DATTUTDUT using 5 m resolution data to agree well with measurements on DOY 100, 163 and 218, but not on DOY 162 and DOY 219 when the ET extremes may not have been readily present or captured in the imagery (see discussion below).

Fig. 8 shows the locations of the extreme T_R pixels selected according to the DATTUTDUT modeling approach using 5 m resolution input for the five days. The dark green band in the lower half of the south field (especially obvious in Fig. 8b and 8c) is an old stream bed which is likely to have different soil properties than the surrounding field. For DOY 162 and 219, cold pixels were located at the north vineyard (Fig. 8b and 8e); while for DOY 163 and 218 just one day later or earlier than DOY 162 and 219, cold pixels were located within this former stream bed or at the tree pixel near the parking lot to the north (Fig. 8c and 8d). Hot pixels were all located in bare soil pixels near the parking lot or in the north field without vines.

In addition to the issues related to the selection of the T_R end-members, DATTUTDUT does not consider effects of aerodynamic resistance (surface roughness) on the heat exchange for a given surface-air temperature difference. A similar finding was reported by French et al. (2005), where they found bias for H from TSEB was typically within 35 W m^{-2}, while bias for H from SEBAL could reach up to 150 W m^{-2}. Nevertheless, the simpler DATTUTDUT modeling scheme is much easier to apply to an image without *a priori* knowledge or skill required. This is a significant benefit in operational, realtime applications. Moreover as shown by Timmermans et al. (2015), output of fluxes from DATTUTDUT often were in good agreement with flux tower measurements and resulting flux fields had patterns consistent with more physically-based models including TSEB and SEBAL.

Using measured S_d from the towers instead of computing from the sun-earth astronomical relationships routinely applied by DATTUTDUT, there is only a minor reduction in the differences with the tower fluxes. An overall improvement in DATTUTDUT estimation of LE is achieved by adopting TSEB estimates of R_n and G (see Table 5). This is particularly true for the north vineyard (site 1). However, even with this better agreement in estimated LE, the discrepancies with observed LE from DATTUTDUT is still larger than with the output of TSEB. This indicates that the errors in available energy using the DATTUTDUT formulations are not the only significant source of error in estimating the LE flux.

4.2 Comparison of spatial patterns in modeled fluxes

Maps of instantaneous EF (assumed to be constant during the day) over the two vineyards are displayed in Fig. 9, along with frequency histograms of daytime ET from the TSEB and DATTUTDUT models expressed in mass units of mm d^{-1}. During IOP1 (DOY 100), the vines were leafing out in early growth stage and the cover crop in the inter-row was the main source of ET. However, the cover crop in the interrow for the north field was mowed shortly before this aircraft overpass, while the cover crop in the south field was unmowed, and was taller and more lush. As a result, EF and daytime ET distribution histograms showed bimodal shape on DOY 100. The histograms become more unimodal in later IOPs as the vine water use begins to dominate total ET.

While spatial patterns of EF from TSEB and DATTUTDUT were quite similar for all the five overpass dates, driven largely by patterns in T_R (see Fig. 8), the magnitudes in EF differ between the models, some days more significantly than others (Fig. 9a-9e). Use of the finer resolution data had generally a minor to moderate effect on the EF and ET distributions except for DOY 163 where the high resolution output indicates a bimodal distribution in EF and ET compared to the unimodal distributions using the 5 m resolution output from DATTUTDAT and TSEB. Since the DATTUTDUT model always scales EF between 0 and 1, results from the DATTUTDUT model generally had a wider distribution in EF compared to TSEB. An example of a clear difference in the width of the EF distribution can be seen for DOY 162 in IOP 2 (Fig. 9g), while for daytime ET, differences in the distributions were quite evident in IOP 2 and IOP 3 (Fig. 9l, 9n and 9o). A similar result was obtained by Choi et al. (2009), who compared turbulent fluxes estimated by METRIC, TIM and TSEB using Landsat imagery over a corn and soybean production region in central Iowa.

Despite similar model agreement in instantaneous ET with the tower measurements using the 5 m resolution data on DOY 100, 163 and 218 for the three IOPs (Fig. 6), there are in some cases where there are significant differences in maps of EF generated by the two models on these days (Fig. 9). EF discrepancies were particularly large on DOY 162 during IOP2 (Fig. 9b), and on DOY 219 during IOP3 (Fig. 9e). These discrepancies are due primarily to model differences in partitioning A between H and LE within these areas, rather than differences in A itself. In particular, DATTUTDUT has less sensitivity to dry aerodynamically rough surfaces, which the

model does not account for; therefore, DATTUTDUT scheme tends to estimate higher EF (Timmermans et al., 2015). Similar spatial discrepancies in model output were reported by Timmermans et al. (2007) and Choi et al. (2009), even though there was good agreement when the models were compared to flux tower measurements. The selection of improper extreme pixels is another crucial factor causing the large discrepancies for the DOY 162 and 219, as analyzed and discussed in Section 4.1.

4.3 Sensitivity of TSEB and DATTUTDUT to the key input, T_R

The sensitivity of the TSEB and DATTUTDUT models to the key input, T_R, was analyzed in order to further investigate the strengths and weaknesses of the two modeling approaches. The aircraft imagery from DOY 163 was selected as a case study since input data were collected in the afternoon (see Table 1) with near maximum radiation and air temperature conditions. Since T_R is the most important input to both TSEB and DATTUTDUT, EF and ET values were calculated with a bias in T_R (± 3 ℃) to evaluate the sensitivity of these two models to absolute accuracy of this key input. The ±3 degree bias in T_R was selected based on a comparison between ground-based and the airborne T_R measurements for IOP 3. For DATTUTDUT, the influence of extreme pixel selection on the computed EF and ET was also investigated. Values of EF and ET were also calculated with a 1 degree deviation in the assigned Tmax/Tmin (±1 ℃). In addition, the values of Tmax/Tmin were selected using the native pixel resolution T_R imagery. Finally, values of Tmax/Tmin were derived from imagery encompassing a larger study area/modeling domain both at the aggregated 5 m pixel resolution and the T_R native (~0.6 m) resolution. Note that for TSEB, using finer resolution T_R would not be consistent with the model formulations for partitioning between soil and canopy convective energy and radiation fluxes and kinetic temperatures. A list of sensivity tests conducted, along with the resulting EF and daytime ET statistics describing model output over the north and south vineyards, is provided in Table 6.

Results for the various tests of sensivity of output from TSEB and DATTUTDUT to biases in T_R inputs indicate that the error/uncertainty in EF and ET estimation can be fairly significant for TSEB (Fig. 10a-10c and Fig. 10l) with an uncertainty in field average ET of ~1 mm day^{-1}, while there is no real impact on the output from DATTUTDUT (Fig. 10d-10f and Fig. 10m). For TSEB, the shape of the ET distribution remains essentially unchanged, just the mean/centroid of

the distribution and max/min ET are shifted. This result is not unexpected based on prior sensitivity studies of both modeling approaches (e.g., Timmermans et al., 2007). The ± 1 degree change in the max/min T_R also does not impact the output of ET with DATTUTDUT (Fig. 10g-10h and Fig. 10n). However, changing the size of the modeling domain for defining max/min T_R and/or the pixel resolution has a measurable impact on the spatially-distributed output from DATTUTDUT in these tests (Fig. 10i-10k and Fig. 10o). Similar to TSEB, the uncertainty in field average ET is ~ 1 mm day^{-1}. With a larger study domain, the selected hot pixel is likely to have higher T_R while the cold pixel will tend to have lower T_R (see Table 6) since the number of pixels available for selection of the extremes are increased. This causes the ET estimation from larger domain (Case D5 and D7) to have a narrower distribution compared to ET from smaller domain (Case D0 and D6) (see Fig. 10o). The finer (native) T_R resolution also results in greater temperature extremes in the hot and cold pixels. (Table 6) since the pixels available for selection of the end-members were less contaminated containing a mixture of canopy and soil/substrate surfaces. Owing to the likely difference LE rates for the bare soil/senscent cover crop versus the irrigated vine vegetation the ET estimation from finer resolution T_R data (Case D6 and D7) tended to be more bimodal than that from courser resolution T_R (Case D0 and D5) (see Fig. 10o).

These tests confirm that simple scaling schemes like DATTUTDUT benefit from insensitivity to biases in T_R, but are sensitive to pixel size and range of conditions present within the modeling domain. This is in contrast to results reported by French et al. (2015), where they concluded that no significant difference in daily ET estimation accuracy was observed running the METRIC model at high (aircraft-based) and medium (Landsat) pixel resolutions. Their study fixed extreme pixels using an objective criteria based on clustered means rather than single pixels, which may reduce the likelihood of an error in selecting an outlier as an extreme hot or cold pixel. Moreover they conducted the inter-comparison of model output at the two resolutions focused on field-averaged ET in comparison to water balance estimates; therefore, the effects on ET distributions or variability were not evaluated in detail. Lastly, the sources of the input data at the two spatial resolutions were provided by the different platforms - aircraft and Landsat; however, the effects of changing the pixel resolution of either the aircraft or satellite data were not evaluated. While more automated approaches are being developed for determining extreme T_R-values in applying contextual-based methods such as METRIC (Morton et al., 2013), the current study demonstrates that pixel resolution of T_R and sampling area will influence the

selection of extreme limits in the approach used by DATTUTDUT, resulting in differences in spatial distribution/patterns in ET from DATTUTDUT within a given study area.

4.4 Water consumption analysis

Water consumption estimates at the field scale provide important information for water management decision making. In this section, estimates of field-scale daytime water consumption for the north and south fields were calculated by aggregating daytime ET totals for all pixels encompassed within each field and then converting to a volume (in liters) by the area of the corresponding field. When using the observed ET (from the flux towers), the field scale water consumption was computed by simply multiplying the tower measured daytime ET (forcing closure by residual) by the area (size) of the vineyard. The volume of water use for each field for the five overpass dates is illustrated in Fig. 11.

The discrepancies between field water consumption from TSEB and DATTUTDUT were relatively small (3% - 6%) on DOY 100, 163 and 218, since the instantaneous and daytime ET estimates from the two models were similar. However, the water use estimated from TSEB was 25% and 33% less than that computed by DATTUTDUT on DOY 162 and 219, respectively. Water consumption calculated by TSEB tended to agree with observed daytime ET estimated from the tower observations, but often had slightly lower ET estimates. This is consistent with the fact that, particularly for the north (site 1) vineyard, the flux tower footprint generally came from the center area of the field with highest EF and ET (cf. Fig. 1 and Fig. 9). On the other hand, DATTUTDUT tended to estimate higher field scale ET than TSEB and tower measurements, particularly on DOY 162 and 219. The overall higher estimated water use for IOP2 and IOP3 by DATTUTDUT is likely due to the simplfied parameterization of heat exchange based solely on T_R and the pixel selection criteria for the hydrologic extremes as analyzed in Section 4.1 and Section 4.2.

Water use from TSEB was separated into soil/inter-row evaporation (E) and vine/vegetation transpiration (T) for each day by assuming the E/T ratio estimated at the aircraft overpass time was constant during the daytime period (see the red lines in Fig. 11). The variation of E between days was smaller than the variability in T, with standard deviations in E of 95 and 55 kiloliters for the north and south fields, respectively, as compared 197 and 173 kiloliters for T. On

average over the 5 days, the E/ET ratios for site 1 and 2 were estimated by TSEB to be ~0.33 and 0.35, respectively. Although observations of E/ET are not available to validate the TSEB estimates of partitioning, other studies in drip-irrigated vineyards report E/ET ratios of ~0.3 ±0.12 (Yunusa et al., 2004; Ferreira et al., 2012; Poblete-Echeverría et al., 2012; Kerridge et al., 2013), indicating TSEB estimates of E/ET partitioning are not unreasonable.

While some level of discrepancy is expected between modeled and measured vineyard water use due to model errors and measurement uncertainties, there are additional factors which may play a role when there appears to be a fairly large difference in water consumption estimated from the tower measurements *versus* the models, particularly with the TSEB model which tends to have better agreement with the tower measurements. The climate in this region is quite arid during the growing season with the drip irrigation being the only water source for the vines. As a result, the water availability (or soil water content) condition in the vine root zone plays a crucial role in the vegetation biomass. Therefore it is reasonable to assume there would be a strong correlation between ET and vine LAI as representative of the water availability in the root zone. The spatial variation in vine LAI is likely due to variation in the amount of irrigated water and/or variability in soil water holding capacity. Specifically, on days like DOY 162 and 163 for the north field and DOY 100 for the south field where there are significant differences between tower observations and TSEB estimates, there are also large differences observed between the LAI within the tower source area and the field average. The lower (higher) LAI of the flux tower source area is associated with the lower (higher) daytime ET estimated from the flux tower observations *versus* the spatially-distributed ET output from the TSEB model. The differences in LAI from the source area and field average are not large (see Table 7), but they do support the idea that a single measurement of water use within a vineyard is not always representative of the total vineyard water consumption.

In a comparison of ET measurements acquired over irrigated cotton eddy covariance, water balance and lysimeters, Kustas et al. (2015) show how variability in LAI within the different source areas associated with each measurement device was correlated to discrepancies between the measured values ET. In the current study, if the ratio of the field *versus* flux tower source area average LAI is used to adjust the water consumption estimates from the ET tower measurements for the two fields, in all cases except one (DOY 100 at site 2) there is closer agreement with TSEB estimates (see Fig. 11). The continued discrepancy for DOY 100 site 2

has more to do with the fact that the G values from the tower site were significantly higher than modeled (see Fig. 6) and are suspect since the ratio of G/R_n for much of the daytime period ranged from 0.3 to 0.45 which are values expected for bare soil (Santanello and Friedl, 2003). This resulted in the daytime available energy R_n-G for the tower site to be ~0.7 of the value estimated by TSEB. Therefore, closure of the tower-based ET flux did not significantly boost the observed value for DOY 100.

With the ET distributions from the models illustrated in Fig. 12, one sees that often the tower measurements fall significantly away from the center/mean of the modeled ET distributions. This is a major advantage with remote sensing-based ET approaches using high pixel resolution data which can capture the actual variation in key surface conditions (vegetation cover, soil moisture) affecting ET. While in most cases the LAI adjustment to the ET tower measurements improved the agreement with model estimated field scale water consumption, the capability of the remote sensing-based surface energy balance models in mapping ET provides a unique tool for identifying areas in the field potentially under water stress conditions. This isn't practical using micrometeorological methods.

Current operational techniques for estimating water use of crops primarily rely on the crop coefficient technique based on the FAO 56 publication (Allen et al., 1998). The actual ET of the crop is estimated by first computing a reference ET (ET_0) which is then multiplied by the crop coefficient (K_C). This single crop coefficient is often divided (called the dual crop coefficient) into a basal crop coefficient (K_{Cb}), which is associated with the crop transpiration and has been related to remotely sensed vegetation indices (Neale et al., 1989) and a soil surface evaporation coefficient (K_e). There is also included a K_s coefficient to reduce crop transpiration for a deficit in water availability in the root zone so the expression has the form $ET=(K_{Cb}K_s + K_e)ET_0$. Determining K_e and K_s requires running a soil water balance model for the surface and root zone. A recent application of this methodology over corn and soybean croplands is given by Gonzalez-Dugo and Mateos (2008) where they find this reflectance-based crop coefficient technique can significantly overestimate ET during a prolonged dry down period. There also appears to be no consistent or universal relationship between crop coefficients and vegetation indices and so this approach is not readily transferable to different crops and climatic conditions (Gonzalez-Dugo et al., 2009).

As an example, the spatial distribution of K_C was computed using FAO 56 estimated ET_0 and the ET map from TSEB from DOY 163 (Fig. 13). There is a significant spatial variation in K_C due in part to the know effect of leaf area/fractional cover (Choudhury et al., 1994), which is seen in the correlation between the K_C map and LAI map of Fig. 4, but there are other factors including the vine variety and the possibility of some level of stress in areas of the vineyard that cannot be reliably detected by this approach. Using the ET measurements from the flux towers and FAO 56 estimated ET_0, for the north vineyard site 1, the value of K_C ranged from 0.55 for DOY 100 to 0.76-0.82 for the other days. For the south vineyard (site 2), K_C values ranged from 0.59 for DOY 100 to 0.62-0.65 for the other days, indicating little variation in K_C with vine phenology. In contrast, the FAO 56 manual recommends K_C values for vineyards at early, peak and end of the growing season of 0.3, 0.7 and 0.45. Clearly, a calibration with this approach is required, which is not only dependent on vine variety but also on vine management (i.e., row orientation and spacing, pruning, irrigation scheduling, etc.)

5 Conclusions

High resolution multispectral and thermal imagery obtained by aircraft mounted sensors were used to map evapotranspiration (ET) over two vineyards in central California using both the Two Source Energy Balance (TSEB) and single-source contextual-based DATTUTDUT (Deriving Atmosphere Turbulent Transport Useful To Dummies Using Temperature) model which scales evaporative fraction (EF) between 0 and 1 using only the radiometric surface temperature (T_R) extemes of cold/wet and hot/dry pixels in the remotely sensed scene. This study focused on five aircraft overpass dates (DOY 100, 162, 163, 218 and 219) over the vine growing season in 2013.

Component soil and canopy temperatures from TSEB agreed well with the airborne-based observationsderived within the flux-tower source-area yielding a bias on the order of 0.5 ℃ and a RMSD-value ~2.5 ℃ for both soil/cover crop and vine canopy temperatures. Instantaneous and daytime integrated fluxes from the TSEB and DATTUTDUT models were validated with flux tower measurements. The TSEB model was able to derive satisfactory estimates of both instantaneous and daytime sensible heat flux (H) and latent heat flux (LE) for all the five overpass dates, while overall the DATTUTDUT model output of H and LE were in less agreement with the tower measurements, particualrly for DOY 162 and 219 overpass dates.

Spatial distributions of evaporative fraction, EF, and daytime ET from the two models were compared for all the five overpass dates. While the spatial patterns of relatively high and low values of EF mapped by TSEB and DATTUTDUT for the two vineyard fields were similar, the magnitude and range in the EF values were quite different on certain days. Specifically, the distributions of EF values from DATTUTDUT often yielded a wider range due to the requirement that each image contains ET at the extremes of potential and ET=0. This resulted in EF and daytime ET magnituides and spatial patterns generated by the two models being fairly similar on DOY 100, 163 and 218, while having larger discrepancies on DOY 162 and 219. In general, inter-comparisons between the performance of TSEB and DATTUTDUT using high resoultion (meter-scale) data tended to yield conclusions consistent with results from prior studies comparing TSEB with single-source models based on contextual scaling of maximum and minimum ET using moderate resolution data (see e.g., French et al., 2005, 2015; Timmermans et al., 2007; Choi et al., 2009). With a more physically-based two-source formulations explicitly treating soil and vegetation energy and radiation exchanges and reliable T_R data, the TSEB model is fairly robust and able to derive reliable ET patterns at sub-field scale under a wide range of environmental conditions. The performance of DATTUTDUT model in computing reliable ET and generating distributions and patterns over the vineyards was similar to TSEB on some of the overpass dates, but for other times the DATTUTDUT model performance was less than satisfactory largely depending on whether there actually existed pixels in the scene that were representative of the extreme ET conditions, namely "maximum" ET (LE=Rn-G) and no ET (LE= 0).

Differences in daytime ET estimated from the two models directly contributes to the discrepancies in field-scale water use estimates, which on certain days was quite significant. The discrepancies in field scale water consumption calculations from the two models ranged from 3% to 33%, which translated to differences in field scale water use between the two models ranging from approximately 68 to 899 kiloliters. Field-scale water consumption estimated from TSEB agreed more closely with estimates based on tower ET observations, while DATTUTDUT tended to estimate higher water use. Disagreement between modeled and measurements is partly due to the difference with LAI of the tower source area and the whole field average. Larger differences in water use occurred when source area LAI failed to represent the field average. A simple adjustment using the ratio of average LAI from the field and the tower source-area greatly

reduced the discrepancy with the TSEB model output. Comparsion between tower measured ET and ET distributions from the models shows that tower measurements generally do not have a value that is representative of the center/mean of the modeled ET distributions.

Compared with water consumption information provided by flux tower observations, the type of spatially-distributed ET information provided by thermal-based energy balance models has clear advantages, particularly when imagery is at fine pixel resolution. ET observed by flux tower is sampling a relatively small area of the field, while the ET models with the T_R imagery can provide spatially-distributed water use information over the entire vineyard and consequently identify the spatial distribution of plant water status, a required input for precision irrigation systems. Two-souce schemes like TSEB are able to provide reliable ET estimation as well as the partitioning between E and T since the model explicitly parameterizes the radiative and convective exchanges between the soil and canopy systems.

However, the senstivity analysis indicates that high-quality T_R input data are needed for TSEB. The DATATTUDUT contextual scaling approach, with automatic pixel selection, is not sensitive to errors in T_R and requires only very basic information as model input, making it relatively easy to apply operationally. Nevertheless, such one-source approaches fail to provide estimates of the E and T partitioning, and the ET estimation at least for DATTUTDUT can be sensitive to domain size and spatial resolution due to the simple model parameterizations.

With UAV technology rapidly developing to provide remote sensing products in near real time (Berni et al., 2009b) , the DATTUTDUT scheme can provide real time ET maps at sub-field scale that will in many cases yield reliable patterns, but not in all cases appropriate magnitudes in ET. In cases where the landscape is aerodynamically rough and dry, an adjustment to the end-member selection for the DATTUTDUT scheme appears to be necessary (Timmermans et al., 2015). If routine high-resolution imagery from UAVs become operational, a hybrid methodology integrating a very simple ET model (DATTUTDUT) with a more robust modeling scheme (TSEB) should be developed. Specifically, if the LST imagery is at fine enough pixel resolution to distinguish soil and vegetation temperatures the DATTUTDUT scheme could be applied separately for the soil and vegetation, providing E and T estimates that could be integrated with TSEB output computed at coarser resolutions or adapted for very fine resolution imagery. Moreover, to ensure continuous and reliable daily water use and vegetation stress

monitoring incorporating the crop coeffcient based technique linked to a water balance model with the thermal-based ET approach using data assimilation has shown utility and addresses to a large extent the shortcomings in estimating/updating the crop coefficient and the impact of plant stress (Neale et al., 2012).

Acknowledgements

Funding provided by E. & J. Gallo Winery made possible the acquisition and processing of the high resolution aircraft imagery used in this study. In addition we would like to thank the staff of Viticulture, Chemistry and Enology Division of E. & J. Gallo Winery, in particular Nick Dokooozlian, Brent Sams, and Martin Mendez-Costabel who made possible the collection of the field validation data . The author, Ting Xia, acknowledges the U.S. Department of Agriculture for hosting her one-year visit to the Hydrology and Remote Sensing Laboratory, and also the China Scholarship Council (CSC) for financially supporting her stay. This work was also financially supported by the National Natural Science Foundation of China via Grant 51279076 and 91125018, and the Twelfth National Key Science & Technology Program of China via Grant 2013BAB05B03.

References：

Allen, R. G., Pereira, L. S., Raes, D., and Smith, M.: Crop evapotranspiration (guidelines for computing crop water requirements). FAO irrigation and drainage paper no. 56. FAO, Rome, Italy; 1998.

Allen, R. G., Tasumi, M., and Trezza, R.: Satellite-based energy balance for mapping evapotranspiration with internalized calibration (METRIC)—Model, J. Irrig. Drain. Eng., 133, 380-394, doi:10.1061/(ASCE)0733-9437(2007)133:4(380), 2007.

Anderson, M. C., Neale, C. M. U., Li, F., Norman, J. M., Kustas, W. P., Jayanthi, H., and Chavez, J.: Upscaling ground observations of vegetation water content, canopy height, and leaf area index during SMEX02 using aircraft and Landsat imagery, Remote Sens. Environ., 92, 447-464, doi:10.1016/j.rse.2004.03.019, 2004.

Anderson, M. C., Allen, R. G., Morse, A., and Kustas, W. P.: Use of Landsat thermal imagery in monitoring evapotranspiration and managing water resources, Remote Sens. Environ., 122, 50-65, doi:10.1016/j.rse.2011.08.025, 2012a.

Anderson, M. C., Kustas, W. P., Alfieri, J. G., Gao, F., Hain, C., Prueger, J. H., Evett, S., Colaizzi, P., Howell, T., and Chávez, J. L.: Mapping daily evapotranspiration at Landsat spatial scales during the BEAREX'08 field campaign, Adv. Water Resour., 50, 162-177, doi:10.1016/j.advwatres.2012.06.005, 2012b.

Bastiaanssen, W. G. M., Menenti, M., Feddes, R. A., and Holtslag, A. A. M.: A remote sensing surface energy balance algorithm for land (SEBAL). 1. Formulation, J. Hydrol., 212, 198-212, doi:10.1016/S0022-1694(98)00253-4, 1998.

Berni, J. A. J., Zarco-Tejada, P. J., Sepulcre-Cantó, G., Fereres, E., and Villalobos, F.: Mapping canopy conductance and CWSI in olive orchards using high resolution thermal remote sensing imagery, Remote Sens. Environ., 113, 2380-2388, doi:10.1016/j.rse.2009.06.018, 2009a.

Berni, J., Zarco-Tejada, P. J., Suárez, L., and Fereres, E.: Thermal and narrowband multispectral remote sensing for vegetation monitoring from an unmanned aerial vehicle, IEEE T. Geosci. Remote, 47, 722-738, doi:10.1109/TGRS.2008.2010457, 2009b.

Brutsaert, W.H.: On a derivable formula for long-wave radiation from clear skies. Water Resour. Res. 11 (5), 742–744, 1975.

Brutsaert, W., and Sugita, M.: Application of self−preservation in the diurnal evolution of the surface energy budget to determine daily evaporation, J. Geophys. Res. Atmos., 97, 18377-18382, doi:10.1029/92JD00255, 1992.

Cammalleri, C., Anderson, M. C., Ciraolo, G., D'Urso, G., Kustas, W. P., La Loggia, G. and Minacapilli, M.: Applications of a remote sensing-based two-source energy balance algorithm for mapping surface fluxes without in situ air temperature observations, Remote Sens. Environ., 124, 502–515, doi:10.1016/j.rse.2012.06.009, 2012.

Cammalleri, C., Anderson, M. C., Gao, F., Hain, C. R., and Kustas, W. P.: A data fusion approach for mapping daily evapotranspiration at field scale, Water Resour. Res., 49, 4672-4686, doi:10.1002/wrcr.20349, 2013.

Cammalleri, C., Anderson, M. C., and Kustas, W. P.: Upscaling of evapotranspiration fluxes from instantaneous to daytime scales for thermal remote sensing applications, Hydrol. Earth Syst. Sci., 18, 1885-1894, doi:10.5194/hess-18-1885-2014, 2014.

Campbell, G.S., and Norman. J.M.: An introduction to environ- mental biophysics, Springer-Verlag New York, New York, 1998.

Carlson, T.N.; Gillies, R.R., and Perry, E.M.: A Method to Make Use of Thermal Infrared Temperature and NDVI measurements to Infer Surface Soil Water Content and Fractional Vegetation Cover, Remote Sensing Reviews, 9, 161-173, doi:10.1080/02757259409532220, 1994.

Carlson, T. N., and Ripley, D. A.: On the relation between NDVI, fractional vegetation cover, and leaf area index, Remote Sens. Environ., 62, 241-252, doi:10.1016/S0034-4257(97)00104-1, 1997.

Carlson, T.: An overview of the" Triangle Method" for estimating surface evapotranspiration and soil moisture from satellite imagery, Sensors, 7, 1612-1629, doi:10.3390/s7081612, 2007.

Choi, M., Kustas, W. P., Anderson, M. C., Allen, R. G., Li, F., and Kjaersgaard, J. H.: An intercomparison of three remote sensing-based surface energy balance algorithms over a corn

and soybean production region (Iowa, US) during SMACEX, Agr. Forest Meteorol., 149, 2082-2097, doi:10.1016/j.agrformet.2009.07.002, 2009.

Choudhury, B. J., Ahmed, N. U., Idso, S. B., Reginato, R. J., and Daughtry, C. S. T.: Relations between evaporation coefficients and vegetation indices studied by model simulations, Remote Sens. Environ., 50, 1–17, doi: 10.1016/0034-4257(94)90090-6, 1994.

Colaizzi, P. D., Kustas, W. P., Anderson, M. C., Agam, N., Tolk, J. A., Evett, S. R., Howell, T.A., Gowda, P.H., and O'Shaughnessy, S. A.: Two-source energy balance model estimates of evapotranspiration using component and composite surface temperatures, Adv. Water Resour., 50, 134-151, doi:10.1016/j.advwatres.2012.06.004, 2012a.

Colaizzi, P. D., Evett, S. R., Howell, T. A., Li, F., Kustas, W. P., and Anderson, M. C.: Radiation Model for Row Crops: I. Geometric View Factors and Parameter Optimization, Agron. J., 104, 225-240, doi:10.2134/agronj2011.0082, 2012b.

Crago, R. D.: Conservation and variability of the evaporative fraction during the daytime, J. Hydrol., 180, 173-194, doi:10.1016/0022-1694(95)02903-6, 1996.

Evett, S. R., Kustas, W. P., Gowda, P. H., Anderson, M. C., Prueger, J. H., and Howell, T. A.: Overview of the Bushland Evapotranspiration and Agricultural Remote sensing EXperiment 2008 (BEAREX08): A field experiment evaluating methods for quantifying ET at multiple scales, Adv. Water Resour., 50, 4-19, doi:10.1016/j.advwatres.2012.03.010, 2012.

Ferreira, M.I., Silvestre, J., Conceição, N., and Malheiro, A.C.: Crop and stress coefficients in rainfed and deficit irrigation vineyards using sap flow techniques, Irrig. Sci., 30, 433–447, doi:10.1007/s00271-012-0352-2, 2012.

Feng, J., and Wang, Z.: A satellite-based energy balance algorithm with reference dry and wet limits, Int. J. Remote Sens., 34, 2925-2946, doi:10.1080/01431161.2012.748990, 2013.

French, A. N., Jacob, F., Anderson, M. C., Kustas, W. P., Timmermans, W., Gieske, A., Su, Z., Su, H., McCabe, M.F., Li, F., Prueger, J., and Brunsell, N.: Surface energy fluxes with the Advanced Spaceborne Thermal Emission and Reflection radiometer (ASTER) at the Iowa 2002 SMACEX site (USA), Remote Sens. Environ., 99, 55-65, doi:10.1016/j.rse.2005.05.015, 2005.

French, A. N., Hunsaker, D. J., and Thorp, K. R.: Remote sensing of evapotranspiration over cotton using the TSEB and METRIC energy balance models, Remote Sens. Environ., 158, 281-294, doi:10.1016/j.rse.2014.11.003, 2015.

Fuentes, S., De Bei, R., Pech, J., and Tyerman, S.: Computational water stress indices obtained from thermal image analysis of grapevine canopies, Irrig. Sci., 30, 523-536, doi:10.1007/s00271-012-0375-8, 2012.

Gao, F., Anderson, M. C., Kustas, W. P., and Wang, Y.: Simple method for retrieving leaf area index from Landsat using MODIS leaf area index products as reference, J. Appl. Remote Sens., 6, 063554-1, doi:10.1117/1.JRS.6.063554, 2012.

Gardner, B. R., Blad, B. L., and Watts, D. G.: Plant and air temperatures in differentially-irrigated corn, Agr. Meteorol., 25, 207-217, doi:10.1016/0002-1571(81)90073-X, 1981.

Gonzalez-Dugo, M. P., and Mateos, L.: Spectral vegetation indices for benchmarking water productivity of irrigated cotton and sugarbeet crops, Agric. Water Manage., 95, 48–58, doi:10.1016/j.agwat.2007.09.001, 2008.

Gonzalez-Dugo, M. P., Neale, C., Mateos, L., Kustas, W. P., Prueger, J. H., Anderson, M. C., and Li, F.: A comparison of operational remote sensing-based models for estimating crop evapotranspiration, Agric. Forest Meteorol., 149, 1843-1853, doi:10.1016/j.agrformet.2009.06.012, 2009.

Gonzalez-Dugo, V., Zarco-Tejada, P., Berni, J. A., Suarez, L., Goldhamer, D., and Fereres, E.: Almond tree canopy temperature reveals intra-crown variability that is water stress-dependent, Agr. Forest Meteorol., 154, 156-165, doi:10.1016/j.agrformet.2011.11.004, 2012.

Hsieh, C. I., Katul, G., and Chi, T. W.: An approximate analytical model for footprint estimation of scalar fluxes in thermally stratified atmospheric flows, Adv. Water Resour., 23, 765-772, doi:10.1016/S0309-1708(99)00042-1, 2000.

Jackson, R. D., Reginato, R. J., and Idso, S. B.: Wheat canopy temperature: a practical tool for evaluating water requirements, Water Resour. Res., 13, 651-656, doi:10.1029/WR013i003p00651, 1977.

Jackson, R. D., Idso, S. B., Reginato, R. J., and Pinter, P. J.: Canopy temperature as a crop water stress indicator, Water Resour. Res., 17, 1133-1138, doi:10.1029/WR017i004p01133, 1981.

Jiang, L., and Islam, S.: A methodology for estimation of surface evapotranspiration over large areas using remote sensing observations, Geophys. Res. Lett., 26, 2773-2776, doi:10.1029/1999GL006049, 1999.

Kalma, J. D., McVicar, T. R., and McCabe, M. F.: Estimating land surface evaporation: A review of methods using remotely sensed surface temperature data, Surv. Geophys., 29, 421-469, doi:10.1007/s10712-008-9037-z, 2008.

Kerridge, B.L., Hornbuckle, J.W., Christen, E.W., and Faulkner, R.D.: Using soil surface temperature to assess soil evaporation in a drip irrigated vineyard, Agric. Water Manag., 116, 128–141, doi:10.1016/j.agwat.2012.07.001, 2013.

Kustas, W. P., and Norman, J. M.: Use of remote sensing for evapotranspiration monitoring over land surfaces, Hydrolog. Sci. J., 41, 495-516, doi:10.1080/02626669609491522, 1996.

Kustas, W. P., and Norman, J. M.: Evaluation of soil and vegetation heat flux predictions using a simple two-source model with radiometric temperatures for partial canopy cover, Agr. Forest Meteorol., 94, 13-29, doi:10.1016/S0168-1923(99)00005-2, 1999.

Kustas, W. P., and Norman, J. M.: A two-source energy balance approach using directional radiometric temperature observations for sparse canopy covered surfaces, Agron. J., 92, 847-854, doi:10.2134/agronj2000.925847x, 2000.

Kustas, W., and Anderson, M.: Advances in thermal infrared remote sensing for land surface modeling, Agr. Forest Meteorol., 149, 2071-2081, doi:10.1016/j.agrformet.2009.05.016, 2009.

Kustas, W.P., Anderson, M.C., Prueger, J.H., Alfieri, J.G., McKee, L.G., Xia, T., Sanchez, L., Geli, H., and Neale, C.M.U.: Utility of Thermal Remote Sensing for Evapotranspiration Estimation of Vineyards [abstract], American Meteorological Society's 31st Conference on Agricultural and Forest Meteorology, Portland, OR, USA, 12-15 May 2014, Available at: https://ams.confex.com/ams/31AgF2BioGeo/webprogram/Paper246963.html, last access: 16 October 2015, 2014.

Kustas, W. P., Alfieri, J. G., Evett, S., and Agam, N.: Quantifying variability in field-scale evapotranspiration measurements in an irrigated agricultural region under advection, Irrig. Sci., 33, 325-338, doi: 10.1007/s00271-015-0469-1, 2015.

Leinonen, I., and Jones, H. G.: Combining thermal and visible imagery for estimating canopy temperature and identifying plant stress, J. Exp. Bot., 55, 1423-1431, doi:10.1093/jxb/erh146, 2004.

Li, F., Kustas, W. P., Prueger, J. H., Neale, C. M., and Jackson, T. J.: Utility of remote sensing-based two-source energy balance model under low-and high-vegetation cover conditions, J. Hydrometeorol., 6, 878-891, doi:10.1175/JHM464.1, 2005.

Li, F., Kustas, W. P., Anderson, M. C., Prueger, J. H., and Scott, R. L.: Effect of remote sensing spatial resolution on interpreting tower-based flux observations, Remote Sens. Environ., 112, 337-349, doi:10.1016/j.rse.2006.11.032, 2008.

Long, D., and Singh, V. P.: A two-source trapezoid model for evapotranspiration (TTME) from satellite imagery, Remote Sens. Environ., 121, 370-388, doi:10.1016/j.rse.2012.02.015, 2012.

Long, D., and Singh, V. P.: Assessing the impact of end−member selection on the accuracy of satellite−based spatial variability models for actual evapotranspiration estimation, Water Resour. Res., 49, 2601-2618, doi:10.1002/wrcr.20208, 2013.

Masek, J. G., Vermote, E. F., Saleous, N. E., Wolfe, R., Hall, F. G., Huemmrich, K. F., Gao, F., Kutler, J., and Lim, T. K.: A Landsat surface reflectance dataset for North America, 1990-2000, IEEE Geosci. Remote S. Lett., 3, 68-72, doi:10.1109/LGRS.2005.857030, 2006.

Morton, C. G., Huntington, J. L., Pohll, G. M., Allen, R. G., McGwire, K. C., and Bassett, S. D.: Assessing calibration uncertainty and automation for estimating evapotranspiration from agricultural areas using METRIC, J. Am. Water. Resour. As., 49, 549-562, doi:10.1111/jawr.12054, 2013.

Neale, C. M. U., Bausch, W., and Heermann, D.: Development of reflectance based crop coefficients for corn, Trans. ASAE, 32, 1891–1899, 1989.

Neale, C. M. U., Geli, H. M. E., Kustas, W. P., Alfieri, J. G., Gowda, P. H., Evett, S. R., Prueger, J. H., Hipps, L. E., Dulaney, W. P., Chavez, J. L., French, A. N., and Howell, T. A.: Soil water content estimation using a remote sensing based hybrid evapotranspiration modeling approach, Adv. Water Resour., 50, 152-161, doi:10.1016/j.advwatres.2012.10.008, 2012.

Norman, J. M., Kustas, W. P., and Humes, K. S.: Source approach for estimating soil and vegetation energy fluxes in observations of directional radiometric surface temperature, Agr. Forest Meteorol., 77, 263-293, doi:10.1016/0168-1923(95)02265-Y, 1995.

Poblete-Echeverría, C., Ortega-Farias, S., Zuñiga, M., and Fuentes, S.: Evaluation of compensated heat-pulse velocity method to determine vine transpiration using combined measurements of eddy covariance system and microlysimeters, Agr. Water Manage., 109, 11-19, doi:10.1016/j.agwat.2012.01.019, 2012.

Roerink, G. J., Su, Z., and Menenti, M.: S-SEBI: a simple remote sensing algorithm to estimate the surface energy balance, Phys. Chem. Earth, 25, 147-157, doi:10.1016/S1464-1909(99)00128-8, 2000.

Ryu, Y., Baldocchi, D. D., Black, T. A., Detto, M., Law, B. E., Leuning, R., Miyata, A., Reichstein, M., Vargas, R., Ammann, C., Beringer, J., Flanagan, L., Gu, L. H., Hutley, L. B., Kim, J., McCaughey, H., Moors, E. J., Rambal, S., and Vesala, T.: On the temporal upscaling of evapotranspiration from instantaneous remote sensing measurements to 8-day mean daily-sums, Agr. Forest Meteorol., 152, 212-222, doi:10.1016/j.agrformet.2011.09.010, 2012.

Santanello Jr, J. A., and Friedl, M. A.: Diurnal covariation in soil heat flux and net radiation, J. Appl. Meteorol., 42, 851-862, doi:10.1175/1520-0450(2003)042<0851:DCISHF>2.0.CO;2, 2003.

Sánchez, L., Mendez-Costabel, M., Sams, B., Morgan, A., Dokoozlian, N., Klein, L. J., Hinds, N., Hamann, H. F., Claassen, A., and Lew, D.: Effect of a variable rate irrigation strategy on the variability of crop production in wine grapes in California. 12th International Conference on Precision Agriculture, Sacramento, CA, USA, 20-23 July 2014, Available:. https://www.ispag.org/presentation/3/1582/, last access: 30 July 2015, 2014.

Smith, G. M., and Milton, E. J.: The use of the empirical line method to calibrate remotely sensed data to reflectance, Int. J. Remote Sens., 20, 2653-2662, doi:10.1080/014311699211994, 1999.

Song, L., Liu, S., Kustas, W. P., Zhou, J., Xu, Z., Xia, T., and Li, M.: Application of remote sensing-based two-source energy balance model for mapping field surface fluxes with composite and component surface temperatures, Agr. Forest Meteorol., Under review.

Su, Z.: The Surface Energy Balance System (SEBS) for estimation of turbulent heat fluxes, Hydrol. Earth Syst. Sci., 6, 85-99, doi:10.5194/hess-6-85-2002, 2002.

Timmermans, W. J., Kustas, W. P., Anderson, M. C., and French, A. N.: An intercomparison of the surface energy balance algorithm for land (SEBAL) and the two-source energy balance (TSEB) modeling schemes, Remote Sens. Environ., 108, 369-384, doi:10.1016/j.rse.2006.11.028, 2007.

Timmermans, W. J., Kustas, W. P., and Andreu, A.: Utility of an automated thermal-based approach for monitoring evapotranspiration, Acta Geophys., doi:10.1515/acgeo-2015-0016, online pu, 2015.

Twine, T. E., Kustas, W. P., Norman, J. M., Cook, D. R., Houser, P., Meyers, T. P., Prueger, J. H., Starks, P. J., and Wesely, M. L.: Correcting eddy-covariance flux underestimates over a grassland, Agr. Forest Meteorol., 103, 279-300, doi:10.1016/S0168-1923(00)00123-4, 2000.

Yang, Y., and Shang, S.: A hybrid dual - source scheme and trapezoid framework–based evapotranspiration model (HTEM) using satellite images: Algorithm and model test, J. Geophys. Res. Atmos., 118, 2284-2300, doi:10.1002/jgrd.50259, 2013.

Yunusa, I.A.M., Walker, R.R., and Lu, P.: Evapotranspiration components from energy balance, sapflow and microlysimetry techniques for an irrigated vineyard in inland Australia, Agric. For. Meteorol., 127, 93–107, doi:10.1016/j.agrformet.2004.07.001, 2004.

Zarco-Tejada, P. J., González-Dugo, V., and Berni, J. A.: Fluorescence, temperature and narrow-band indices acquired from a UAV platform for water stress detection using a micro-hyperspectral imager and a thermal camera, Remote Sens. Environ., 117, 322-337, doi:10.1016/j.rse.2011.10.007, 2012.

Zarco-Tejada, P. J., González-Dugo, V., Williams, L. E., Suárez, L., Berni, J. A., Goldhamer, D., and Fereres, E.: A PRI-based water stress index combining structural and chlorophyll effects: Assessment using diurnal narrow-band airborne imagery and the CWSI thermal index, Remote Sens. Environ., 138, 38-50, doi:10.1016/j.rse.2013.07.024, 2013.

Zhang, L., and Lemeur, R.: Evaluation of daily evapotranspiration estimates from instantaneous measurements, Agric. For. Meteorol., 74, 139-154, doi:10.1016/0168-1923(94)02181-I, 1995.

Zipper, S. C., and Loheide II, S. P.: Using evapotranspiration to assess drought sensitivity on a subfield scale with HRMET, a high resolution surface energy balance model, Agric. For. Meteorol., 197, 91-102, doi:10.1016/j.agrformet.2014.06.009, 2014.

Tables：

Table 1. Flight and pixel resolution information concerning the images obtained from the airborne campaigns.

IOP	Date (DOY)	Flight time (UTC)	Original spatial resolution (m)		Flight height (m)
			Multispectral	Thermal	
1	April 10 (100)	18:29-18:43	0.09	0.7	430
2	June 11 (162)	18:20-18:26	0.05	0.42	240
2	June 12 (163)	21:11-21-16	0.05	0.38	240
3	August 6 (218)	18:34-18:37	0.1	0.66	480
3	August 7 (219)	18:46-18:49	0.1	0.65	480

Table 2. Difference statistics describing comparisons between modeled fluxes from TSEB and DATTUTDUT at the overpass time and observations (original and with adjustments using the RE and BR methods for energy balance closure) (W m^{-2}).

Site	Flux	DOY No.	Mean Obs.	TSEB (5 m pixel res.)			DATTUTDUT (5 m pixel res.)			DATTUTDUT (native pixel res.)		
				Bias	MAE	RMSD	Bias	MAE	RMSD	Bias	MAE	RMSD
Site 1	R_n	5	593	0	26	33	-43	64	66	-61	61	65
	G	5	85	5	28	33	-18	35	40	-24	35	38
	H	5	195	13	37	42	48	53	68	41	57	68
	LE	5	268	-63	70	87	-117	117	150	-123	139	157
	LE_{RE}	5	313	-18	32	37	-73	76	105	-78	100	106
	H_{BR}	5	215	33	55	62	68	71	89	61	76	91
	LE_{BR}	5	293	-38	50	58	-92	94	125	-98	119	129
Site 2	R_n	5	590	6	15	23	-19	26	27	-40	40	42
	G	5	132	41	43	59	6	47	61	12	42	55
	H	4	195	-23	43	45	8	31	39	21	53	59
	LE	4	186	-90	90	102	-106	106	119	-149	149	163
	LE_{RE}	4	253	-23	43	51	-38	55	63	-81	90	101
	H_{BR}	4	231	13	33	48	44	59	68	57	81	90
	LE_{BR}	4	217	-59	61	77	-74	77	93	-117	117	136

Table 3. Difference statistics describing comparisons between modeled daytime fluxes from TSEB and DATTUTDUT model and observations (original and with adjustments using the RE and BR methods) (MJ m^{-2} d^{-1}).

Site	Flux	DOY No.	Mean Obs.	TSEB (5 m pixel res.)			DATTUTDUT (5 m pixel res.)			DATTUTDUT (native pixel res.)		
				Bias	MAE	RMSD	Bias	MAE	RMSD	Bias	MAE	RMSD
Site 1	R_n-G	5	15.0	-0.5	0.7	0.9	-1.2	1.2	1.5	-1.2	1.4	1.6
	H	5	4.4	-1.0	1.2	1.4	-0.1	1.0	1.2	-0.1	1.2	1.3
	LE	5	8.5	-1.6	1.6	1.8	-3.2	3.2	3.6	-3.1	3.2	3.6
	LE_{RE}	5	10.6	0.5	1.0	1.1	-1.1	1.4	1.9	-1.0	1.9	2.0
	H_{BR}	5	9.9	4.4	4.4	5.1	5.4	5.4	6.1	5.4	5.4	6.0
	LE_{BR}	5	5.1	-4.9	4.9	5.4	-6.6	6.6	7.1	-6.5	6.5	6.9
Site 2	R_n-G	5	13.9	-1.4	1.5	1.9	-1.1	1.5	2.3	-1.7	2.0	2.5
	H	4	5.2	-1.8	1.8	2.2	-0.8	1.1	1.3	-0.3	1.1	1.3
	LE	4	6.2	-2.6	2.6	2.9	-3.1	3.1	3.5	-4.3	4.3	4.6
	LE_{RE}	4	8.8	0.0	1.7	1.7	-0.5	1.7	1.8	-1.6	2.2	2.3
	H_{BR}	4	7.6	0.6	1.9	1.9	1.6	1.6	1.8	2.1	2.1	2.3
	LE_{BR}	4	6.4	-2.4	3.0	3.4	-2.9	2.9	3.4	-4.0	4.0	4.2

Table 4. Difference statistics for daytime ET (MJ m^{-2} d^{-1}) extrapolated from instantaneous estimates using observed available energy *A* (Obs. *A*) from flux towers versus using incoming solar radiation measurements (S_d).

Site	Stat	TSEB		DATTUTDUT	
		Obs. *A*	S_d	Obs. *A*	S_d
Site 1	Bias	0.5	-1.4	-1.1	-3.4
	MAE	1.0	1.4	1.4	3.4
	RMSD	1.1	1.6	1.9	4.1
Site 2	Bias	0.0	-0.8	-0.5	-1.3
	MAE	1.7	1.5	1.7	1.3
	RMSD	1.7	1.8	1.8	1.8

Table 5. Difference statistics comparing instantaneous output of LE from TSEB and DATTUTDUT with current DATTUTDUT algorithms for estimating the available energy versus using the estimates from TSEB.

Site	Flux	DOY No.	Mean Obs.	TSEB			DATTUTDUT (5m)			DATTUTDUT using R_n and G from TSEB		
				Bias	MAE	RMSD	Bias	MAE	RMSD	Bias	MAE	RMSD
Site 1	H	5	195	13	37	42	48	53	68	52	59	75
	LE	5	268	-63	70	87	-117	117	150	-101	101	123
	LE_{RE}	5	313	-18	32	37	-73	76	105	-56	56	77
	H_{BR}	5	215	33	55	62	68	71	89	72	77	96
	LE_{BR}	5	293	-38	50	58	-92	94	125	-76	76	97
Site 2	H	4	195	-23	43	45	8	31	39	1	30	37
	LE	4	186	-90	90	102	-106	106	119	-114	114	123
	LE_{RE}	4	253	-23	43	51	-38	55	63	-47	47	59
	H_{BR}	4	231	13	33	48	44	59	68	37	46	62
	LE_{BR}	4	217	-59	61	77	-74	77	93	-83	83	95

Table 6. Statistics describing EF and daytime ET produced by TSEB and DATTUTDUT over the north and south vineyards for each sensitivity test described in the text.

Model	Cases	Input setting	T_R of extreme limits (℃)		EF					Daytime ET (mm)					
			*T*max	*T*min	Mean[1]	Med.[2]	Std.[3]	Max.[4]	Min.[5]	Mean	Med.	Std.	Max.	Min.	RMSD[6]
TSEB	T0	Original Input	-	-	0.61	0.62	0.12	0.91	0.01	4.3	4.4	1.0	6.8	0.1	0.6
	T1	T_R+3	-	-	0.46	0.48	0.14	0.80	0.02	3.2	3.3	1.1	5.9	0.1	2.0
	T2	T_R-3	-	-	0.73	0.74	0.11	0.99	0.02	5.3	5.3	1.0	7.6	0.1	0.3
DATTUTDUT	D0	Original Input	54.7	31.4	0.67	0.67	0.11	1	0	4.5	4.5	1.3	8.9	0	0.5
	D1	T_R+3	57.7	34.4	0.67	0.67	0.11	1	0	4.4	4.3	1.2	8.7	0	0.6
	D2	T_R-3	51.7	28.4	0.67	0.67	0.11	1	0	4.7	4.6	1.3	9.1	0	0.4
	D3	*T*max+1	55.7	31.4	0.68	0.68	0.11	1	0.04	4.7	4.6	1.2	8.9	0.1	0.4
	D4	*T*min-1	54.7	30.4	0.64	0.64	0.11	0.96	0	4.3	4.2	1.2	8.3	0	0.8
	D5	Whole Area	58.4	23.4	0.55	0.55	0.08	0.77	0.11	3.4	3.3	0.8	5.9	0.3	1.6
	D6	Native Resolution	58.5	25.7	0.62	0.64	0.17	1	0	4.2	4.2	1.8	9.3	0	0.7
	D7	Whole Area and Native Resolution	61.4	20.3	0.57	0.58	0.13	0.87	0.07	3.6	3.6	1.4	7.4	0.2	1.3

[1]Mean: mean of the EF or ET distribution

[2]Med.: median of the EF or ET distribution

[3]Std.: Standard deviation of the EF or ET distribution

[4]Max.: Maximum value of the EF or ET distribution

[5]Min.: Minimum value of the EF or ET distribution

[6]RMSD: the RMSD of the modeled daytime ET at Site 1 and Site 2, $RMSD = \{[(O_1-M_1)^2+(O_2-M_2)^2]/2\}^{1/2}$.

Table 7. Average leaf area index (LAI) estimated for the flux tower source area/flux footprint versus the whole field derived from the aircraft imagery (NDVI relationship with LAI). The LAI values in bold are associated with the days where differences in water consumption estimated by TSEB versus using the tower measured ET are significant for site 1 (North vineyard) and site 2 (South vineyard).

Site	DOY	LAI	
		Source Area	Whole Field
1	100	1.3	1.3
	162	**2.0**	**1.5**
	163	**1.8**	**1.5**
	218	1.6	1.5
	219	1.7	1.5
2	100	**1.7**	**1.9**
	162	1.5	1.5
	163	1.5	1.5
	218	1.2	1.2
	219	1.3	1.2

Figures:

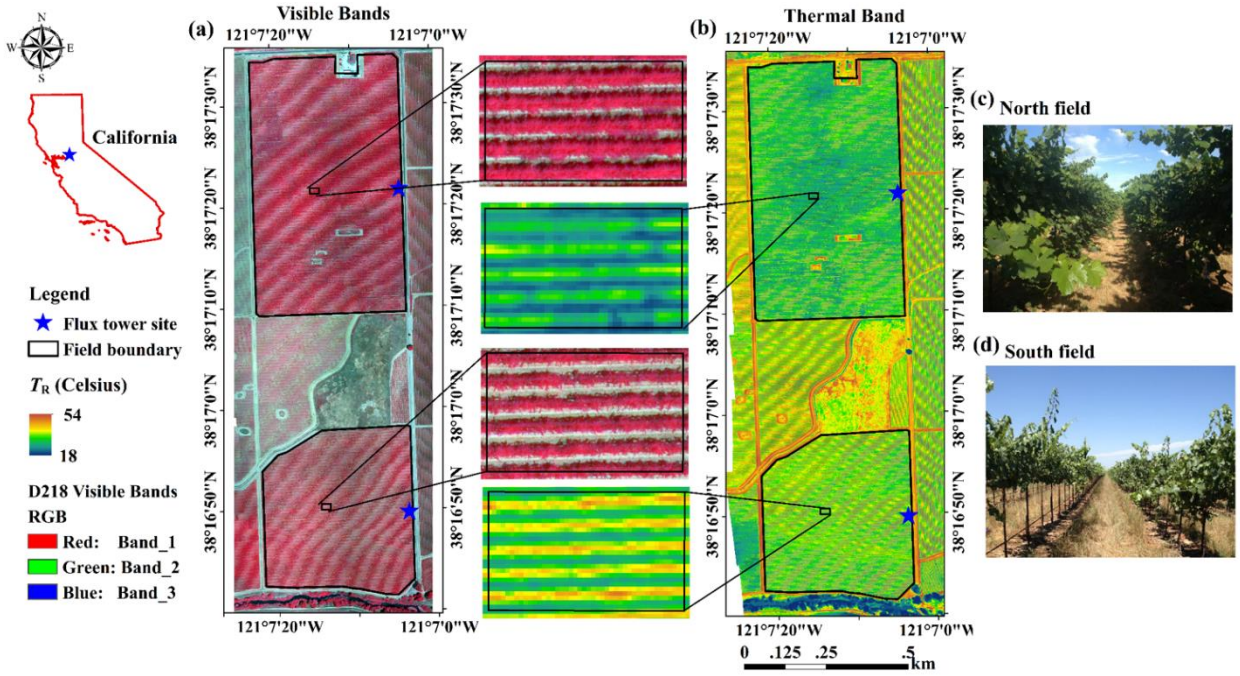

Figure 1. Location of study area overlaid on a false color composite of near-infrared (NIR), red, and green bands with 0.1 m spatial resolution (a) and thermal band with 0.66 m spatial resolution (b) obtained by aircraft on August 6, DOY 218, 2013. In the visible band image (a), red and gray colors denote the vine and bare soil/senescent cover crop in the inter-row, respectively, while in the thermal band image (b), blue/green and yellow/red colors represent vine and bare soil/senescent cover crop in the inter-row, respectively. The black line denotes the boundary of north and south fields, and the blue stars are the locations of the flux tower sites. The two photos of the north and south fields (c and d) were taken on June 11 in 2014 after vines had fully leafed out.

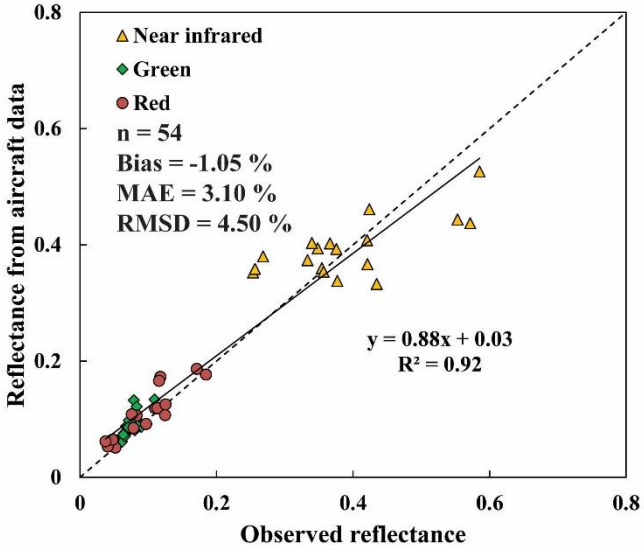

Figure 2. Comparison between observed (*O*) and modeled (*M*) visible band reflectance. The statistics (for the sample size *n*=54) listed in the figure are the Bias (Σ (*O*-*M*)/n), mean absolute error (MAE=$\Sigma|O-M|/n$) and root mean square difference (RMSD=$[\Sigma(O-M)^2/n]^{1/2}$) where the symbol Σ represents a summation over the sample size *n*.

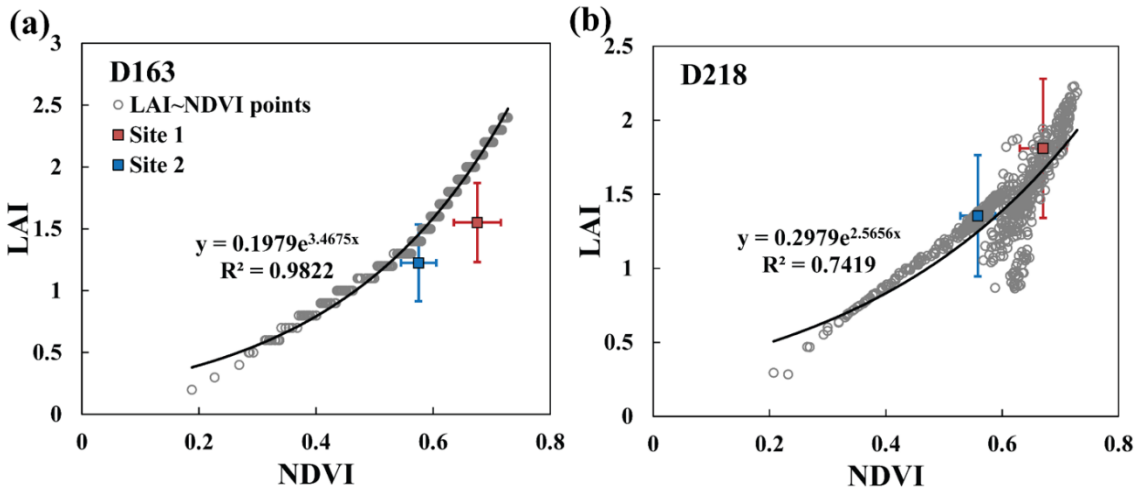

Figure 3. Validation of the LAI~NDVI relation using the ground-based LAI measurements on DOY 163 and 218.

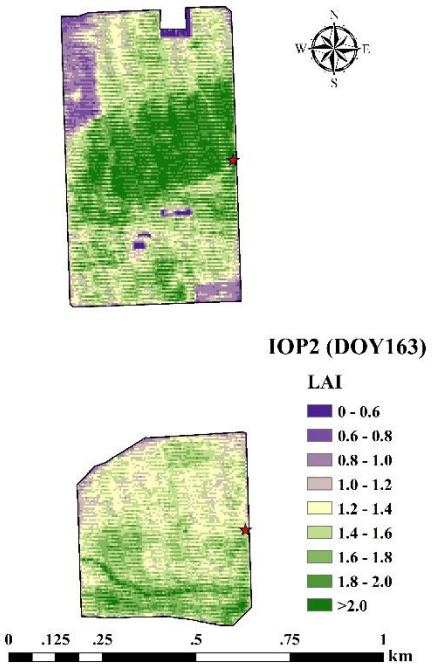

Figure 4. The LAI map generated from the NDVI image for IOP 2 DOY 163.

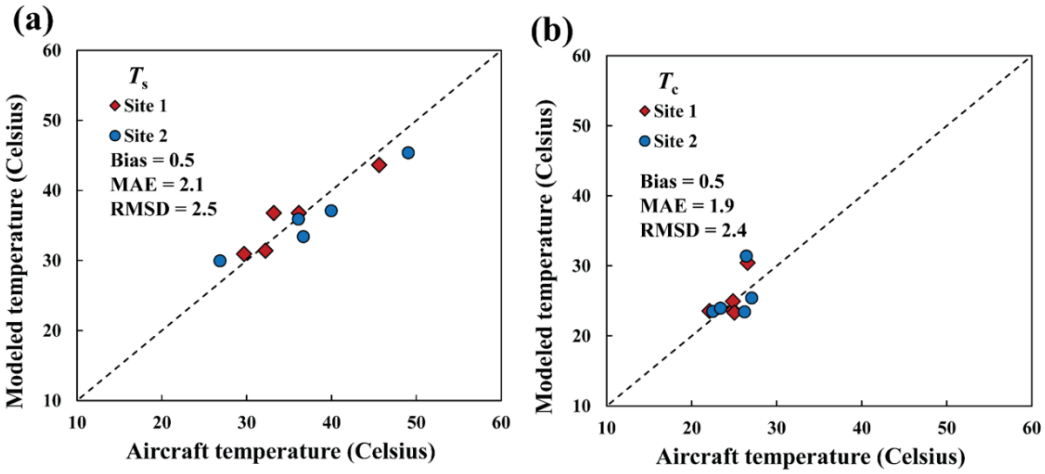

Figure 5. Comparison between modeled T_s and T_c from TSEB and values extracted from the aircraft imagery on the five acquisition days. All the statistics (Bias, MAE and RMSD) have units of ℃.

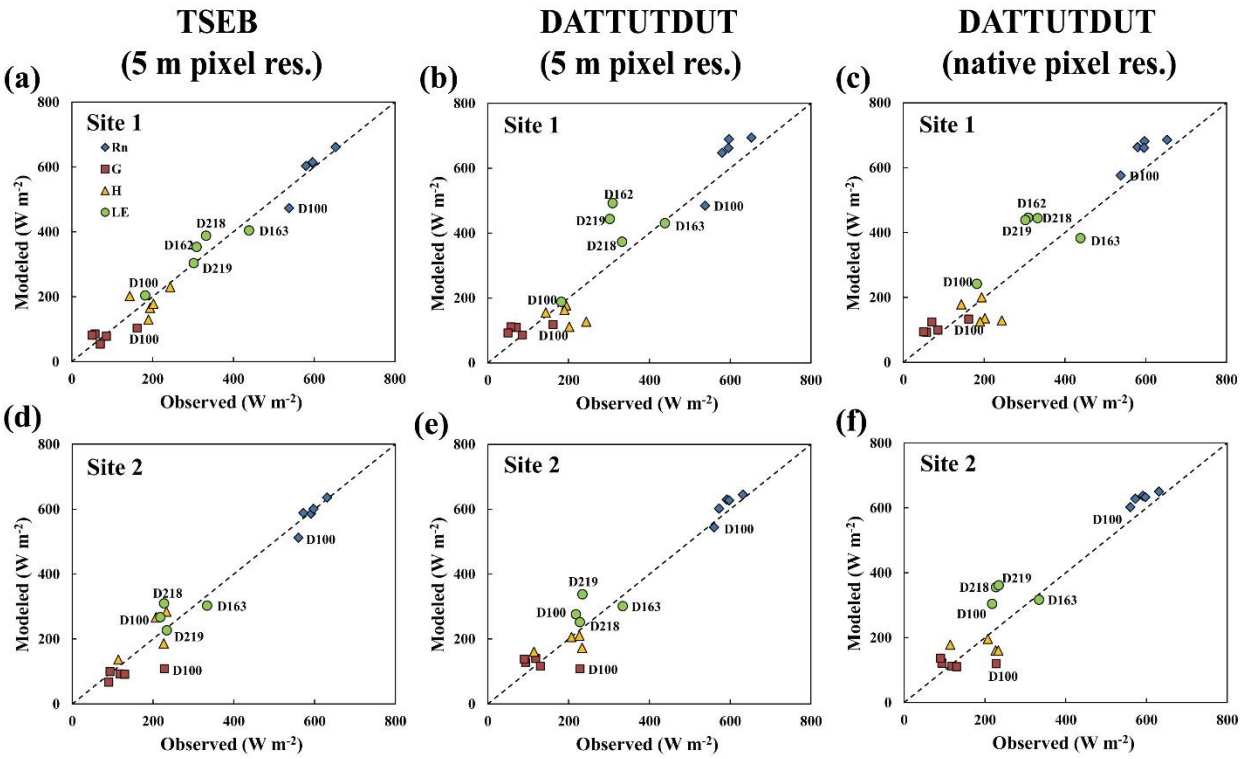

Figure 6. Scatter plot of observed and modeled fluxes from (a) TSEB (5 m pixel resolution), (b) DATTUTDUT (5 m pixel resolution) and (c) DATTUTDUT (native pixel resolution) at the aircraft overpass time for the five days in 2013. The observed *H* and LE use the RE method for energy balance closure. Note for DOY 162, there were no flux data from site 2 due to an EC sensor malfunction.

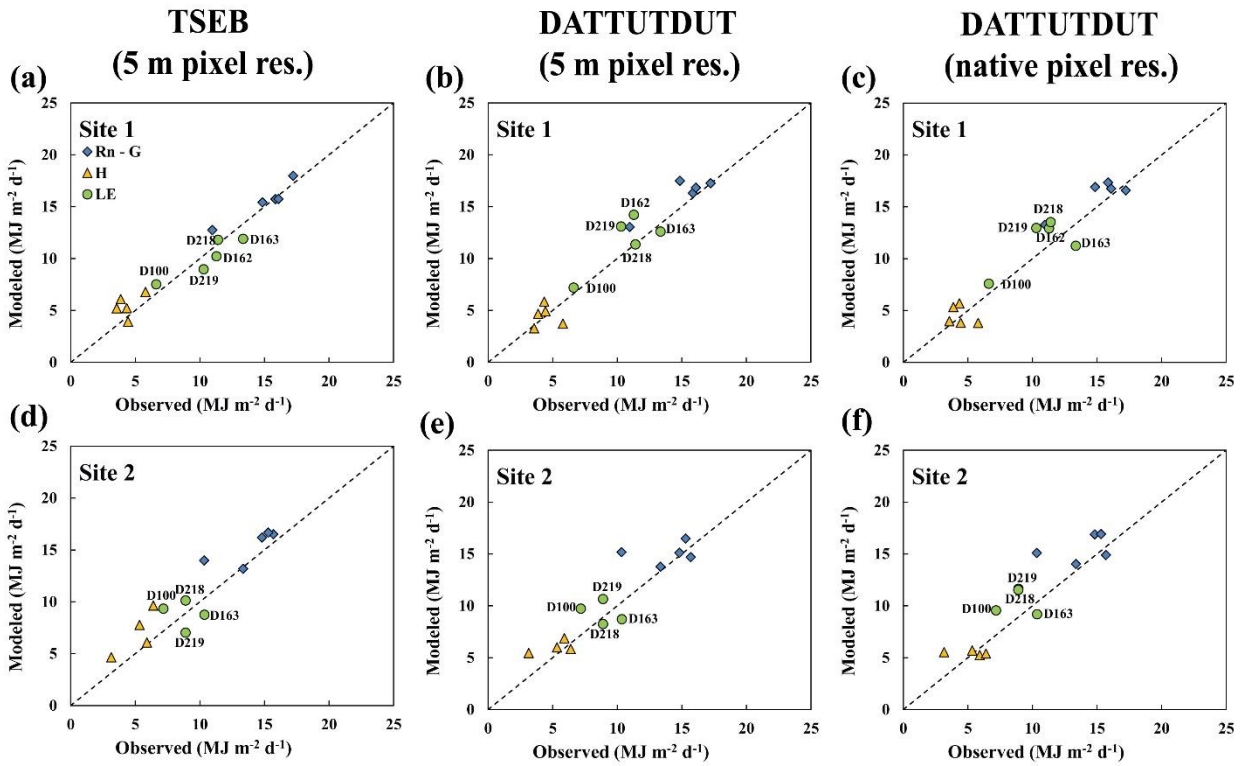

Figure 7. Scatter plot of observed and modeled daytime fluxes from (a) TSEB (5 m pixel resolution), (b) DATTUTDUT (5 m pixel resolution) and (c) DATTUTDUT (native pixel resolution) for the five days in 2013. The observed energy components are adjusted for energy balance using the RE method.

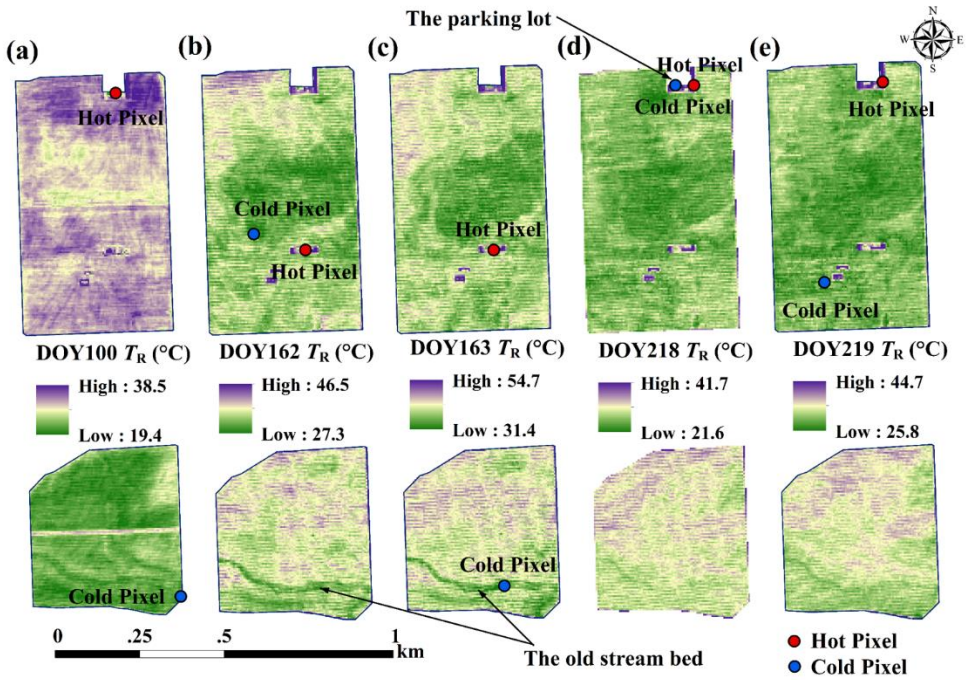

Figure 8. Locations of hot (red points) and cold (blue points) pixels selected from the T_R maps for DATTUTDUT model on the five days.

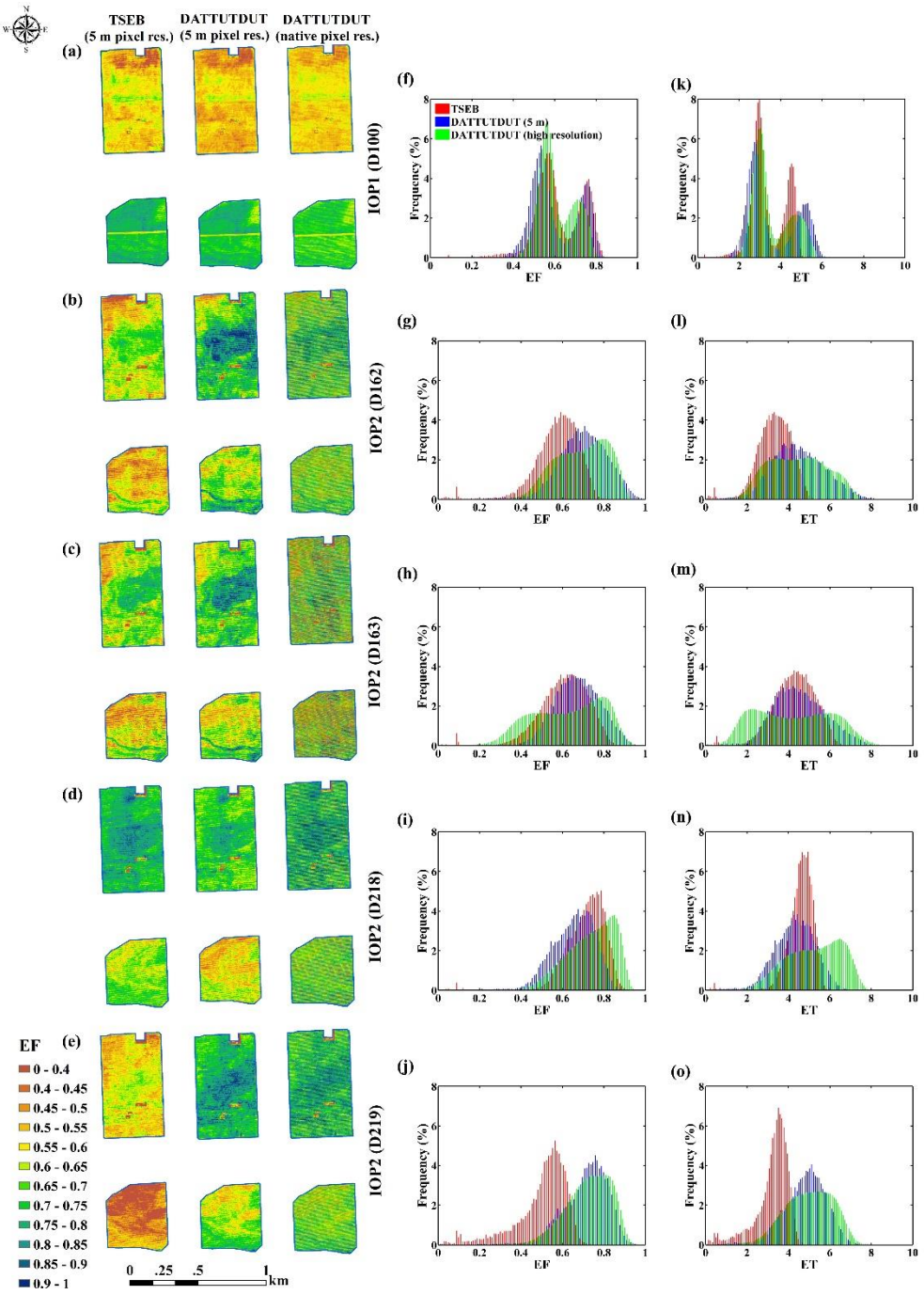

Figure 9. Comparison of TSEB (5 m resolution) and DATTUTDUT model output at 5 m and native pixel resolution: spatial distribution of instantaneous EF (a to e), frequency histogram of instantaneous EF (f to j) and daytime ET (k to o).

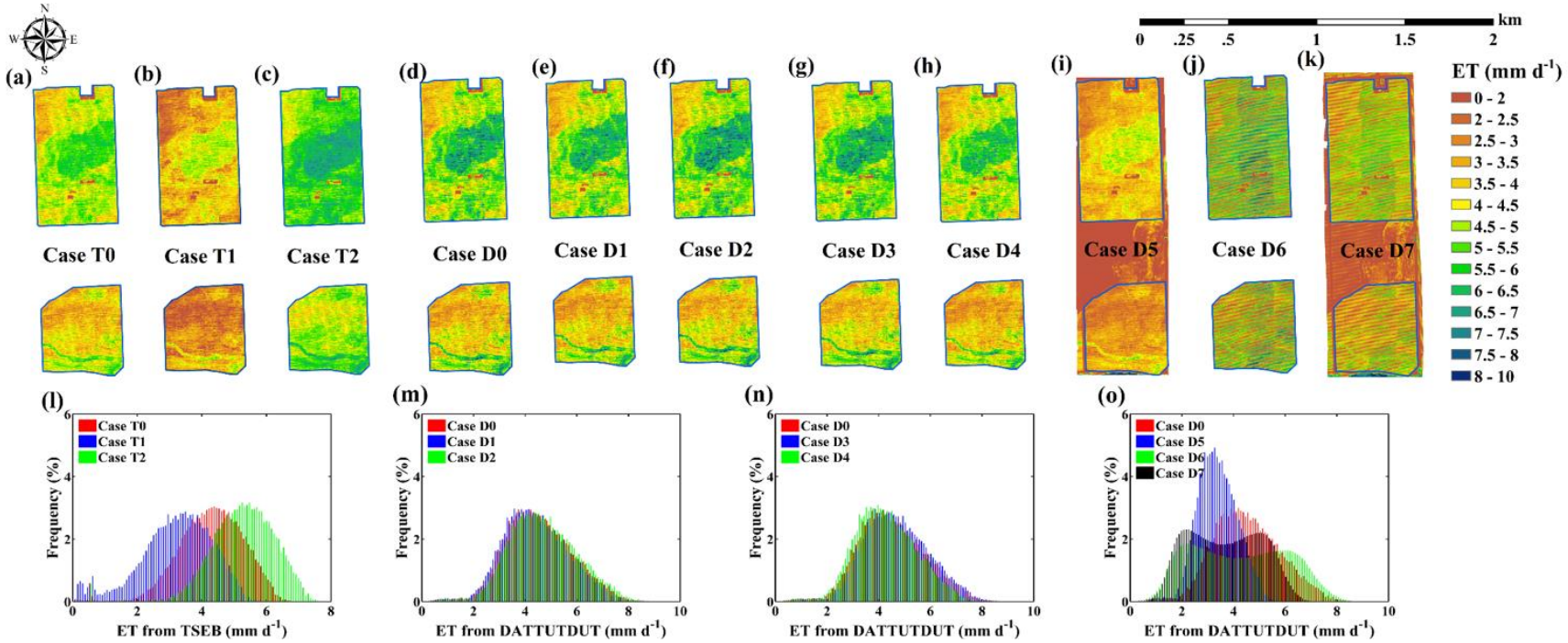

Figure 10. Comparison of the ET patterns and frequency distributions generated by TSEB and DATTUTDUT under the sensitivity tests described in Table 6.

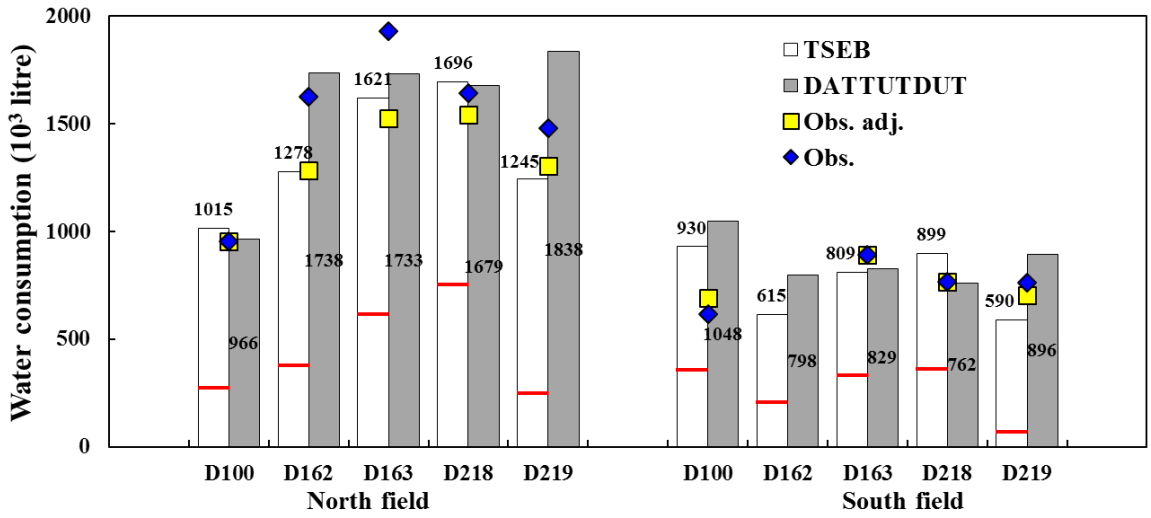

Figure 11. Water consumption calculated from estimates of ET computed by TSEB and DATTUTDUT models for the five aircraft overpass days (10^3 liter). The numerical values above or in the columns denote the total water consumption from each field as estimated by the two models. For results from TSEB, the red lines separate the total water consumption into soil evaporation below the lines and vegetation transpiration above the lines. The blue diamonds denote the water consumption calculated using the EC tower-based daytime ET observed (Obs.) multiplied by the area of the north and south vineyards. The yellow squares are the water consumption values from ET Obs. adjusted (adj.) by multiplying ET Obs. by the ratio of the tower source area LAI and the whole field average LAI.

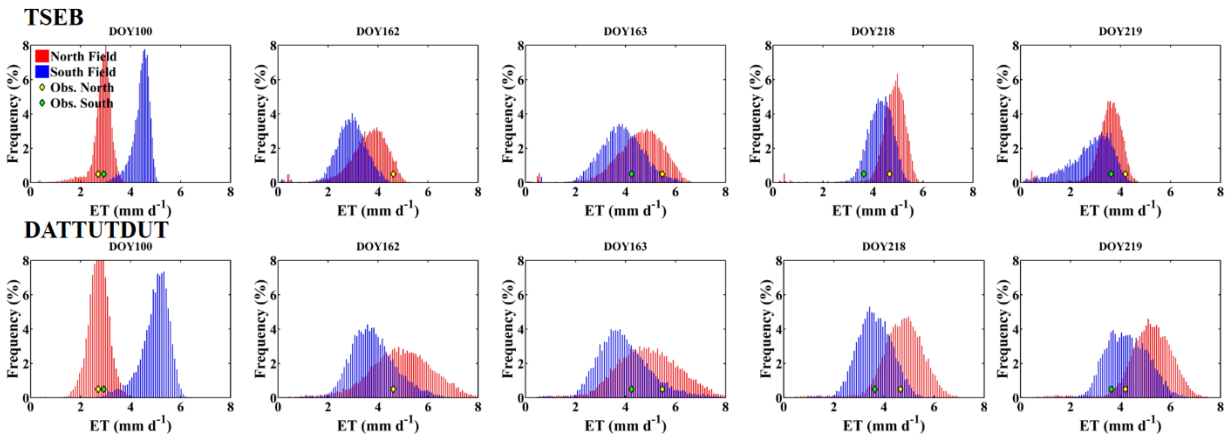

Figure 12. Histograms of output of spatially distributed daytime ET estimated from the TSEB and DATTUTDUT with the daytime ET values from the flux towers identified in the distributions by a yellow and green diamond for the north and south vineyards, respectively.

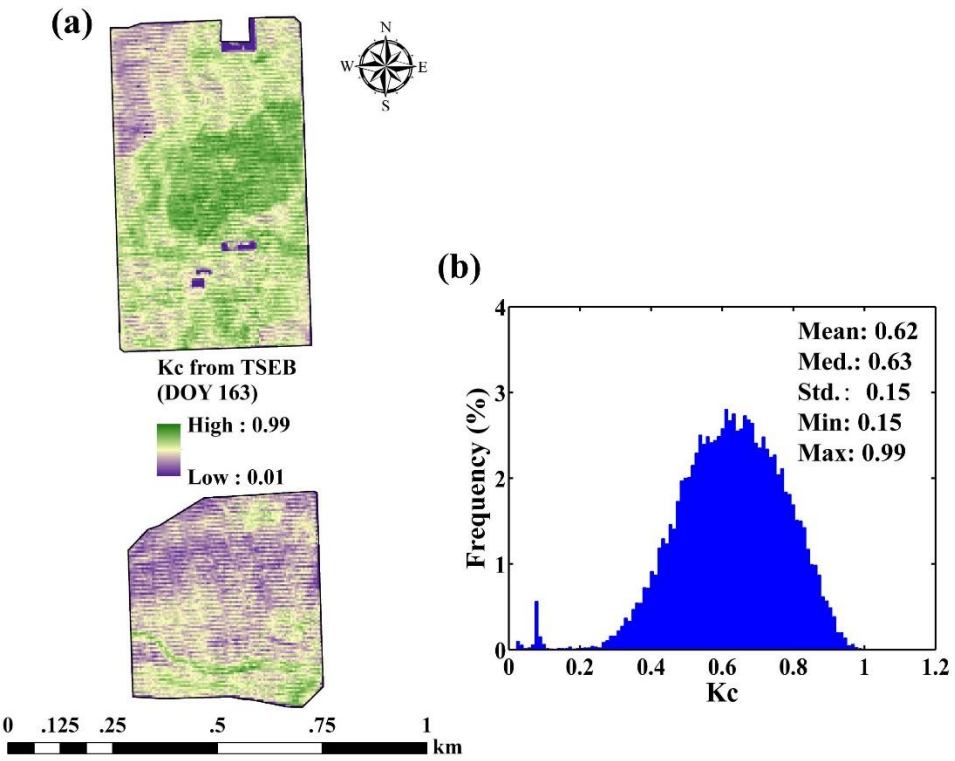

Figure 13. Spatial variation in the crop coefficient Kc computed using TSEB output of ET and ET_0 computed from FAO56 for DOY 163 imagery (a). Also the frequency distribution in Kc for the image is illustrated (b).